OPEN ACCESS Freely available online

CC BY

J. Mcquillan, M. Van Walstijn, J. D. Parker, and M. Ortiz,
"Physical Modeling of a Spring Reverb Tank Incorporating Helix Angle, Damping, and Magnetic Bead Coupling,"
J. Audio Eng. Soc., vol. 73, no. 6, pp. 312–330 (2025 Jun.).
https://doi.org/10.17743/jaes.2022.0199.

Physical Modeling of a Spring Reverb Tank Incorporating Helix Angle, Damping, and Magnetic Bead Coupling

JACOB MCQUILLAN,[1]* MAARTEN VAN WALSTIJN,[1] JULIAN D. PARKER,[2] AND MIGUEL ORTIZ[1]
(jmcquillan15@qub.ac.uk) (m.vanwalstijn@qub.ac.uk) (julian.parker@cantab.net) (m.ortiz@qub.ac.uk)

[1]*SARC: Centre for Interdisciplinary Research in Sound and Music, Queen's University Belfast, Belfast, UK*
[2]*Stability AI, London, UK*

Reproducing the main features of a spring reverb tank impulse response across the hearing range with a physical model presents unique challenges because of the high levels of coupling between the spring's vibrational polarizations. Previous attempts based on a model that includes helix angle can accurately simulate helical spring vibrations but see discrepancies in reproducing measured impulse responses due to heavy simplifications in specifying boundary conditions and input/output mechanisms. This paper presents an improved physical modeling approach by incorporating magnetic bead dynamics and frequency-dependent damping. The beads are modeled as coupled beams using a thin form of the spring equations that reduces to thin beam equations in the absence of curvature. Also ensuring the correct geometric alignment between the beads and the spring, the model's response to rotationally driving the input bead is shown to display the expected mixture of waves traveling along the different spring polarizations. To achieve a similar damping profile as observed in measured impulse responses, different damping parameters are set for each polarization, leading to nonproportional damping and multiple decay rates within small frequency bands. The new formulation results in the main features of measured impulse responses now being reproduced well.

0 INTRODUCTION

Spring reverb is an electromechanical audio effect initially designed as a means of adding reverberation to Hammond organs in the 1930s [1]. Thanks to design optimizations reducing its size and improving practicality, the effects unit eventually saw integration into guitar amplifiers around the 1960s [2–4]. Ever since, it has been enduringly popular as an audio effect across various genres of music—notable examples include *surf rock*, where spring reverb is a staple of the electric guitar tone, and *dub reggae* for its extensive application to percussive elements of tracks, including the use of spring tanks as instruments through direct impulsive excitation of the springs [5].

The emergence of spring reverb as an iconic sound effect in its own right stems from the highly dispersive nature of wave propagation in helical springs, which was an unintended feature at the time of the original Hammond organ design. As a consequence, the repeating echoes building up in the helical spring impart specific timbral qualities beyond introducing reverberation, which sets spring reverb apart from related technologies (e.g., plate reverb or echo chambers).

Assuming the vibrations to be dominantly linear for typical driving levels in reverb tanks, the effects unit is fully characterized by its impulse response. Visualized in Fig. 1 for the reverb tank pictured in Fig. 3, the dispersive behavior of helical springs is evidenced through various overlapping sets of frequency-dependent echoes—these are the hallmarks of the response and often referred to as *chirps*. Tank impulse responses can be split broadly in two regions bordered by a transition frequency f_T [6]: in Fig. 1 this value is just below 5 kHz. Other features below f_T include weaker sets of chirps appearing between the main pattern and gradual blurring of the structured echoes over time. Above the transition frequency, less dispersive sets of echoes with faster transmission times than the main chirps are visible.

Despite the vibrational linearity of reverb tanks, digital emulation has proven challenging due to distributed coupling along the helical spring causing highly dispersive

*To whom correspondence should be addressed, email: jmcquillan15@qub.ac.uk.

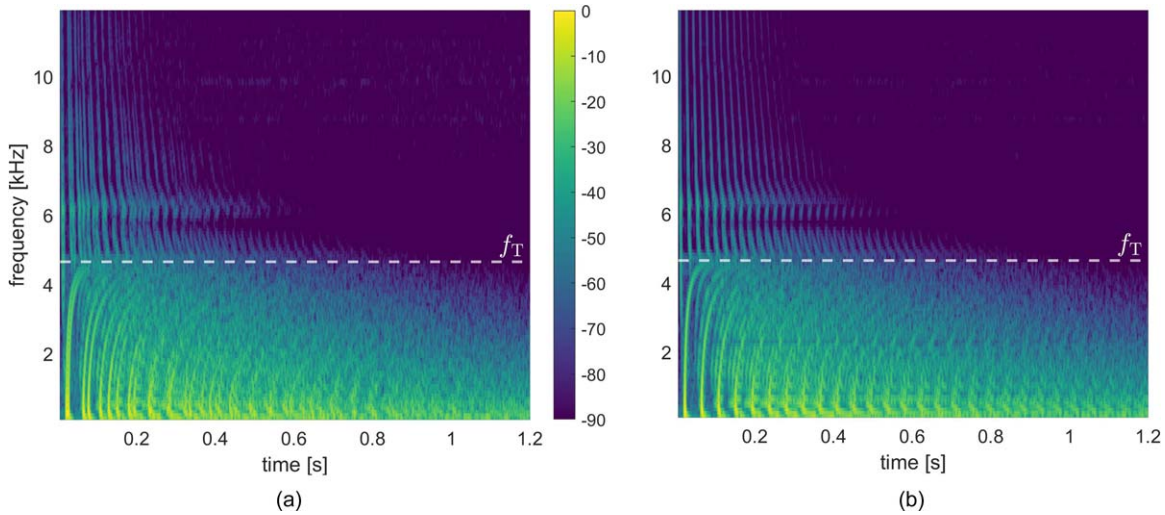


Fig. 1. Spring reverb tank model 2EB2C1B impulse response (a) and the response of a single spring (b). Dashed white lines indicate transition frequency f_T [6].

wave propagation and is still an active area of research. One approach reproduces the main characteristic chirps using a modal structure starting from a simple formula for natural frequencies based on torsional wave propagation along the helical spring [7, 8]. The resultant algorithms are computationally efficient and closed-form expressions for modal parameters allow real-time control. However, while these approaches capture the dispersive behavior of echoes well, they are limited in scope in that only the main chirps below the transition frequency are modeled.

Other paths taken in [9, 10] again aim to reproduce the main features appearing in measured impulse responses, this time proposing a gray-box approach using chains of all-pass filters and delay lines. Adaptations in [11] to the proposed structure see considerable efficiency gains such that it is better suited to a real-time implementation, and automated calibration using measured tank responses in [12] can then set model parameters such that simulated responses see a close match to measurements.

Similar to the modal structures, this approach is both computationally efficient and well suited to parametric control of practical reverberation settings. One drawback is that it is not clear how a link between model parameters and the material and geometry of spring reverb tanks could be established. This is desirable from a design point of view, as discussed in [13, 14]. Such models could be used to develop simulation algorithms, as is proposed in this paper, or alternatively to generate training data for black-box deep learning approaches [15, 16].

Developing a simulation algorithm that can include control over the material and geometry of a reverb tank requires a physics-based approach. Past research using such white-box methodologies is categorized by two starting points: one using a helical spring model derived as an extension of Timoshenko beam vibrations to include curvature [17] and another with a simpler helical spring model [18]. The main simplification in the latter is modeling only one transverse polarization (see u_c and v_c in Fig. 4), and it is thus valid only for springs of low curvature such that the two are effectively degenerate [14].

Based on the notion that typical geometries of springs in reverb tanks make this a reasonable choice, the simple helical spring model has served as the basis for several past digital simulation attempts. In [6], finite difference time domain methods are proposed for a direct numerical implementation of the equations, and extensions are presented in [14], including proposing a family of schemes as a means of reducing numerical dispersion in the discretization process.

Another extension proposed in [14] is attaching a mass-spring at each end of the helical spring to capture the effects of magnetic beads acting as drivers/pick-ups in tanks. Simulating an impulse response using this model sees several features of the accompanying measurement captured well, in particular the shape of the main chirps. However, due to the lower-order accuracy of the employed difference operators, a downside of this approach is that it struggles with accuracy over the relevant frequency range at standard audio rates. This pushes real-time implementations out of reach and also gives rise to some discrepancies in the comparison seen in the reproduction of secondary chirps and temporal blurring.

The difficulties with reducing numerical dispersion are addressed in [13]—instead of a direct implementation, the finite difference scheme is cast to a modal architecture by diagonalizing the eigenvalue problem that forms. As such, finite difference parameters are no longer tied to the simulation algorithm and can be increased with no consequence to the real-time capabilities. This methodology is applied only to the helical spring (i.e., a model for magnetic beads is not incorporated, and instead, the direct access within a modal structure is leveraged to account for the effect of the beads in an ad hoc manner).

By not modeling these effects and opting for a post-processing adjustment, the link between the material and geometry of a tank and the final modal form is diminished. Similar to the other attempts with the simple model,

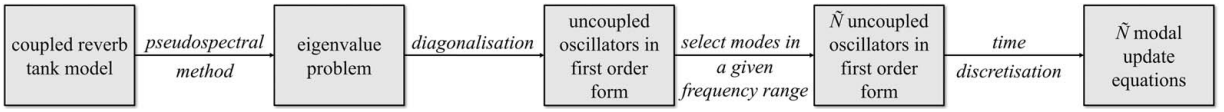


Fig. 2. Overview of deriving a discrete-time modal algorithm from a reverb tank modeled with coupled partial differential equations.

the simulation sees a good match to measurements, now with the main discrepancy being over-prominence of the faint secondary chirps appearing between the main set of echoes. One drawback of this approach lies with extracting the modes from the eigenvalue problem: the modal structure is well suited to a real-time simulation algorithm but online control of model parameters is not trivial since recomputing the modes requires a large matrix diagonalization.

Similar approaches have been developed for simulations based on the more complex helical spring model: one path implementing finite difference time domain schemes [19, 20] and another employing high-order spatial finite difference schemes to cast to a modal form [21]. For both cases, typical geometries of springs in reverb tanks allow the equations to be simplified to a "thin" form of the model (by ignoring Timoshenko effects) while still capturing vibrational behavior in the hearing range [19]. Neither of the past attempts for the "thin spring model" include magnetic beads attached at each end of the spring, and, unlike with the simple spring model, close matches to measured responses have not yet been achieved [20, 21].

It is worth noting that the thin spring model is more unwieldy in reproducing the main features of the tank response because of extra sets of echoes not captured in the simpler model contaminating the output [22]. Regardless, the more faithful representation of the geometry makes extensions to a model that would fully capture the coupling with magnetic beads more viable. Other aspects of the approaches based on the thin spring model that are so far under-researched are modeling loss, in particular the influence physical damping parameters have on modal decay rates, and incorporating axial loading to account for the spring being held under low tension.

To contribute to addressing these shortcomings, this paper aims to achieve a closer match to a measured tank response by incorporating for the first time bead dynamics and damping into a tank model based on a thin spring formulation. Fig. 2 gives a general methodological overview, and the paper is laid out as follows.

How reverb tanks operate is detailed in SEC. 1 and a reverb tank model is then formulated in SEC. 2, with the input and output mechanisms being informed by past experimental work investigating the driving setup in a tank [23]. SEC. 3 details the spatial discretization of said model, which employs the same Chebyshev pseudospectral method as used in earlier studies in application to a helical spring without beads [24, 22]. For completeness, it is noted that several other approaches to physics-based modeling of helical springs were considered (e.g., [25–28]). Ultimately, pseudospectral methods are chosen because they are better suited to modeling connections between magnetic beads and the helical spring. After the modal algorithm is developed in SEC. 4, the model is evaluated in SEC. 5 via comparison with measurement. Conclusions and prospective future work are then discussed in SEC. 6.

1 SPRING REVERB TANK DESIGN AND OPERATION

Spring reverb tanks have seen a few design iterations since they were first built for Hammond organ tone cabinets, though the core concept has endured: helical springs are used as transmission lines aiming to build up echoes akin to reflections in a room [1]. When the delayed signal and its echoes are mixed with the original, it then gives the sound a reverberant character, with the aim that the sense of a physical space is now perceived. Helical springs were chosen for the delay lines to get long enough transmission times in as compact a design as possible and their application is borrowed from an early Bell Laboratories invention related to telecommunications [29].

With the original units being large, expensive to manufacture, and impractical (e.g., springs were fitted in oil-filled tubes), improvements across the board eventually paved the way to the well-known tank design in the 1960s, and this has since been largely unchanged [2–4]. Fig. 3 shows a typical reverb unit that is suspended from four short springs in a metal tank to minimize noise caused by external shock and vibrations.

To get the desired transmission times in a space-efficient setup, springs composed of a thin wire with narrow spacing between coils are fitted between the driving and pick-up transducers and held stretched under low tension [3, 4]. This ensures spacing between the coils is maintained to avoid coil clash and also holds the springs relatively upright rather than letting them freely hang as in an earlier design known as the *necklace reverb* [2]. In the interest of achieving sufficiently high echo density, reverb tanks almost always have more than one transmission spring [2]. The tank in Fig. 3 has two springs operating in parallel, though other designs can have three or also have springs hooked together in a series connection. From a practical perspective, the springs are typically identical apart from the number of coils (i.e., one has a longer wire and thus a different delay time but is stretched to the same coiled length and has the same wire and coil diameter).

The driving unit in tanks as pictured in Fig. 3 is an electromechanical transducer that is fed an input current and generates an electromagnetic field around a small magnetic bead attached to the spring. The electromagnet consists of a coil of wire (into which the input is passed) fitted around a stack of U-shaped metal laminations and the magnetic bead is suspended in the air gap of the U-shape by supporting wires and polarized along its diameter such that the

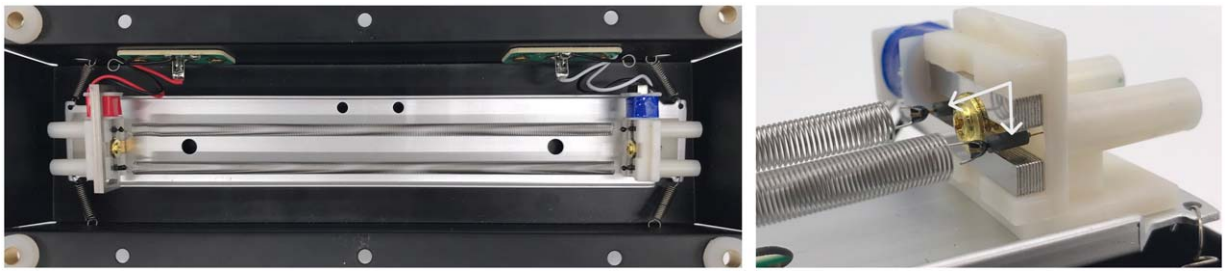


Fig. 3. Spring reverb tank model 2EB2C1B including a close-up of the driving apparatus. White arrows point to magnetic beads.

magnetic field causes it to rotate [2]. The spring and bead are hooked together and bonded securely: with the bead designed to be driven rotationally, one consideration is ensuring the bead is aligned along the center of the spring [4].

The pick-up unit follows the same design principles as the driver, but operating in reverse, with the main difference being the shape of the metal laminations, which is altered to better shield against stray magnetic fields [4]. Based on the principles of electromagnetic induction, an output signal is generated in the coil as a consequence of the change in magnetic flux induced by rotation of the magnetic bead at this end.

2 CONTINUOUS-DOMAIN MODELING

2.1 Helical Spring Vibrations

The geometry of a helical spring is visualized in Fig. 4 and described by its wire radius r (meters), wire length L (meters) along the helix, coil radius R_c (meters), and helix angle α (radians), where α and L are derived from the number of coils and spring length L_c (meters) [30]. These parameters also determine the curvature $\kappa = \cos^2(\alpha)/R_c$ and tortuosity $\tau = \kappa\tan(\alpha)$ of the structure, and for a cylindrical wire, the cross-sectional area $A = \pi r^2$ (square meters) and moment of inertia $I = \pi r^4/4$ (quartic meters) can be defined. The spring material is characterized by its density ρ (kilogram per cubic meter), Young's modulus E (Pascals), Timoshenko shear coefficient γ, and shear modulus $G = E/2(1+\nu)$ (Pascals), where ν is Poisson's ratio.

In lossless form, a linear model of the vibrational behavior along this helical structure is given by Wittrick as a set of 12 coupled equations [17]:

$$\rho A\partial_t^2\mathbf{x} = \mathbf{A}\mathbf{p} + \mathbf{B}\mathbf{q}, \tag{1}$$

$$\mathbf{C}\partial_t^2\mathbf{y} = \mathbf{K}\mathbf{m} - \mathbf{B}\mathbf{p} + \partial_s\mathbf{q}, \tag{2}$$

$$\mathbf{A}\mathbf{x} = \mathbf{H}\boldsymbol{\theta} - \mathbf{B}\mathbf{y} + \frac{\mathbf{p}}{GA\gamma}, \tag{3}$$

$$\partial_s\mathbf{y} = \mathbf{B}\mathbf{x} - \mathbf{K}\boldsymbol{\theta} + \mathbf{J}\mathbf{q}, \tag{4}$$

$$\mathbf{A}\boldsymbol{\theta} = \mathbf{K}^\intercal\mathbf{y} + \frac{\mathbf{m}}{EI}, \tag{5}$$

$$\mathbf{A}\mathbf{m} = \mathbf{H}\mathbf{p} + \mathbf{K}^\intercal\mathbf{q} + \rho I\partial_t^2\boldsymbol{\theta}. \tag{6}$$

The equations are defined for displacements u, v, and w; rotation angles θ_u, θ_v, and θ_w; moments m_u, m_v, and m_w; and forces p_u, p_v, and p_w over time t along the wire-axis coordinate s, with ∂_s^n and ∂_t^n representing nth-order differentiation in space and time, respectively. Each of the vectors in Eqs. (1)–(6) is composed of two variables:

$$\mathbf{x} = \begin{bmatrix} u \\ v \end{bmatrix}, \quad \mathbf{y} = \begin{bmatrix} w \\ \theta_w \end{bmatrix}, \quad \mathbf{p} = \begin{bmatrix} p_u \\ p_v \end{bmatrix},$$
$$\mathbf{m} = \begin{bmatrix} m_u \\ m_v \end{bmatrix}, \quad \boldsymbol{\theta} = \begin{bmatrix} \theta_u \\ \theta_v \end{bmatrix}, \quad \mathbf{q} = \begin{bmatrix} p_w \\ m_w \end{bmatrix}, \tag{7}$$

and the matrices are defined as

$$\mathbf{A} = \begin{bmatrix} \partial_s & -\tau \\ \tau & \partial_s \end{bmatrix}, \quad \mathbf{B} = \begin{bmatrix} \kappa & 0 \\ 0 & 0 \end{bmatrix}, \quad \mathbf{C} = \begin{bmatrix} \rho A & 0 \\ 0 & 2\rho I \end{bmatrix},$$
$$\mathbf{J} = \begin{bmatrix} \frac{1}{EA} & 0 \\ 0 & \frac{1}{2GI} \end{bmatrix}, \ \mathbf{K} = \begin{bmatrix} 0 & 0 \\ -\kappa & 0 \end{bmatrix}, \ \mathbf{H} = \begin{bmatrix} 0 & 1 \\ -1 & 0 \end{bmatrix}. \tag{8}$$

In principle, the effect of axial loading could be incorporated at this stage in the equations following [31]. However, it is not included in the present study due to the difficulty of accurately estimating the load value as well as the minimal effect it appears to have on the result.

For typical geometries of springs found in reverb tanks, it is well established that "thin" versions of Wittrick's 12-variable model comfortably capture vibrations of interest in reverberation applications [19, 20]. The thin spring model with damping used here removes the coupling terms $\mathbf{p}/GA\gamma$ and $\rho I\partial_t^2\boldsymbol{\theta}$ (shown to be negligible in [20]), which allows elimination of eight variables, resulting in a four-variable system [22]:

$$\partial_t^2\mathbf{z} = \mathbf{W}\mathbf{z} - \boldsymbol{\Gamma}\partial_t\mathbf{z}, \quad \mathbf{z} = \begin{bmatrix} u & v & w & \theta_w \end{bmatrix}^\intercal, \tag{9}$$

$$\mathbf{W} = \begin{bmatrix} \mathbf{S} & \mathbf{T} \\ \mathbf{U} & \mathbf{V} \end{bmatrix}, \ \boldsymbol{\Gamma} = \begin{bmatrix} \sigma_u & 0 & 0 & 0 \\ 0 & \sigma_v & 0 & 0 \\ 0 & 0 & \sigma_w & 0 \\ 0 & 0 & 0 & \sigma_\theta \end{bmatrix} - \frac{\eta}{E}\mathbf{W}, \tag{10}$$

where

$$\mathbf{S} = \frac{1}{\rho A}\left(\mathbf{A}\mathbf{Q} + \mathbf{B}\mathbf{N}\right), \quad \mathbf{T} = \frac{1}{\rho A}\left(\mathbf{A}\mathbf{R} + \mathbf{B}\mathbf{P}\right),$$
$$\mathbf{U} = \mathbf{C}^{-1}\left(-EI\mathbf{K}\mathbf{L} - \mathbf{B}\mathbf{Q} + \partial_s\mathbf{N}\right),$$
$$\mathbf{V} = \mathbf{C}^{-1}\left(-EI\mathbf{K}\mathbf{M} - \mathbf{B}\mathbf{R} + \partial_s\mathbf{P}\right), \tag{11}$$

and the submatrices of $\mathbf{W}$ are built using the matrices defined in Eq. (8):

$$\mathbf{M} = \mathbf{A}\mathbf{H}\mathbf{B} + \mathbf{K}^\intercal, \quad \mathbf{N} = \mathbf{J}^{-1}\left(-\mathbf{B} - \mathbf{K}\mathbf{H}\mathbf{A}\right),$$
$$\mathbf{P} = \mathbf{J}^{-1}\left(\mathbf{I}\partial_s - \mathbf{K}\mathbf{H}\mathbf{B}\right), \quad \mathbf{Q} = EI\mathbf{H}\mathbf{A}\mathbf{L} + \mathbf{H}\mathbf{K}^\intercal\mathbf{N},$$
$$\mathbf{R} = EI\mathbf{H}\mathbf{A}\mathbf{M} + \mathbf{H}\mathbf{K}^\intercal\mathbf{P}, \quad \mathbf{L} = \mathbf{A}\mathbf{H}\mathbf{A}, \tag{12}$$

with $\mathbf{I}$ denoting a 2×2 identity matrix.

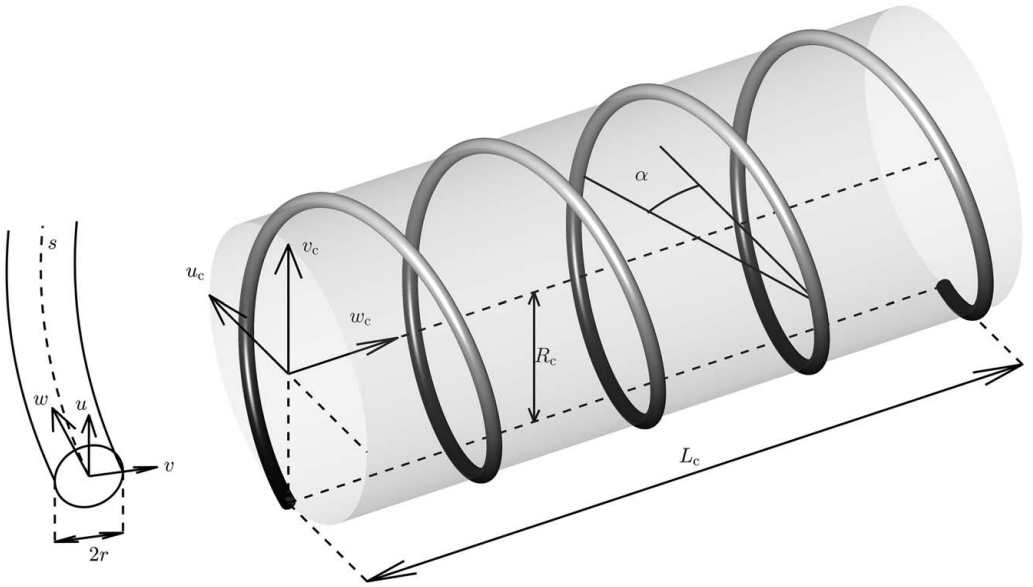


Fig. 4. Helical spring geometry.

The damping matrix $\mathbf{\Gamma}$ is based on a simple loss model considering a Kelvin-Voigt material [32] through the substitution $E \rightarrow E + \eta\partial_t$ (where η represents viscosity) and incorporating frequency-independent loss via parameters σ_u, σ_v, σ_w, and σ_θ. The σ parameters are set differently for each polarization on the physical basis that the surrounding medium affects the transverse ($\sigma_u = \sigma_v$), longitudinal, and rotational wire polarizations differently. In addition, different decay rates appear to exist within narrow frequency ranges in measured impulse responses (e.g., in Fig. 1), further motivating setting different values for each case.

2.1.1 Dispersion Relation

The free wave solution of the lossless thin spring model links temporal frequency ω to wave number β and is derived by inserting the ansatz

$$\mathbf{z} = \mathbf{\Xi} e^{j\omega t + \beta s}, \quad j = \sqrt{-1}, \tag{13}$$

into Eqs. (1)–(6) without the damping terms, where $\mathbf{\Xi}$ is a vector of complex amplitudes. With substitution of the trial solution Eq. (13), derivative operators transform as

$$\partial_t \rightarrow j\omega, \quad \partial_t^2 \rightarrow -\omega^2, \quad \partial_s \rightarrow \beta, \tag{14}$$

and concatenating the system equations then forms an eigenvalue problem that yields eight complex-valued wave numbers for a given frequency. These are composed of four pairs travelling in opposite directions; thus, only positive wave numbers are presented here.

Fig. 5(a) plots frequency against Im(β), which holds propagating wave numbers and illustrates the strong dispersion of waves travelling along a helical spring. The model parameters represent one of the springs in the reverb tank in Fig. 3 and are provided in Table 1 at the start of SEC. 5. Dashed lines represent evanescent waves that are of less interest and thus omitted from Fig. 5(b), and Re(β) is not shown since it holds the exponentially decaying part of wave numbers, which is zero for the lossless case. The hearing range is shaded gray to show that only two dispersion curves are relevant to the hearing range for typical spring geometries found in reverb tanks.

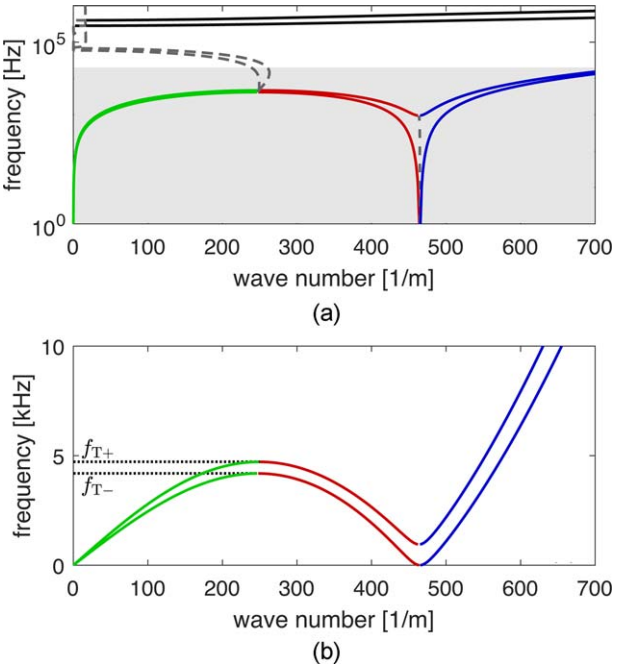


Fig. 5. Plot (a) shows the dispersion relation for the lossless 12-variable Wittrick model [Eqs. (1)–(6)] with solid lines showing propagating waves and dashed lines showing evanescent waves. Plot (b) shows the same dispersion relation on a linear frequency axis, with evanescent waves omitted.

Fig. 5(b) shows the same dispersion relation on a linear frequency axis. The two curves behave similarly, each having a clear transition frequency $f_{T\pm}$ and exhibiting bar-like dispersion at high wave numbers above the transition frequencies (shown in blue) [20]. The color coding reflects grouping helical spring modes by wave number and evaluating the simulated spring impulse response accordingly, which is possible for a finite spring with simple boundary conditions [22]. Each of the three branches of either curve

Table 1. Reverb tank model parameters. Geometric values are directly measured, density values are set for materials specified in [4], and Young's moduli and damping parameters are tuned empirically.

	E (GPa)	ρ (kg/m^3)	L (cm)	r (mm)		Spring 1	Spring 2		Damping
$s_{1,\,9}$	170	8,000	2	0.1	E_5 (GPa)	232	227	σ_u	0.4
$s_{2,\,8}$	0.15	5,000	0.4	0.9	ρ_5 (kg/m^3)	7,800	7,800	σ_v	0.4
$s_{3,\,7}$	E_5	ρ_5	0.5	r_5	r_5 (mm)	0.15	0.15	σ_w	4
$s_{4,\,6}$	E_5	ρ_5	R_c	r_5	R_c (mm)	2.15	2.15	σ_θ	5
					L_5 (m)	4.01	4.76	η	180
					α (degrees)	2.33	1.96		

corresponds to a coherent group of echo patterns in the response of a finite-length spring: green and red to different sets of chirps overlapping in frequency and blue to the more regular sets of echoes most visible above the transition frequencies.

When considering waves along the spring in terms of the global coordinates (u_c, v_c, w_c) in Fig. 4, previous work investigating wave motion in the spring indicates that the upper and lower green curves here correspond to torsional and longitudinal motion along w_c, respectively [27, 33]. In other words, considering this with the input and output being based on magnetic beads rotating about w_c, the main chirps in Fig. 1, which converge to f_{T+}, can be attributed to global rotation along the spring.

2.1.2 Decay Rates

Evaluating the dispersion relation from another angle, one can consider the model in the form of Eq. (9), and inserting the trial solution Eq. (13) now yields a complex frequency $\check{s} = j\omega + \tilde{\alpha}$, where $\tilde{\alpha}$ is the decay rate for a given real-valued wave number. Losses are now included in Eq. (9), and correspondingly, how waves decay with frequency/wave number is shown in Fig. 6. Damping parameters are displayed in Table 1, and the labels $\beta_{T\pm}$ correspond to $f_{T\pm}$ to associate each decay curve with its respective dispersion curve.

The finding that damping as specified here does not yield monotonic relationships between decay rate and frequency/wave number is in alignment with comments made in SEC. 2.1 around observing multiple decay rates in measured impulse responses. Different modes of the same frequency can have very different decay rates, which is remarkable given that the damping profile is conceptually so close to a Rayleigh type [34]. The latter is recovered when all σ parameters are set equal and results in decay rates monotonically increasing with frequency, as, for example, is imposed in [13]. This has important implications for how damping is incorporated into a spring reverb model—there is no clear path to capture the complex decay behavior in an approach that starts from a lossless formulation (e.g., as in [21]).

2.2 Reverb Tank Model

The magnetic beads and supporting wires connected at each end of a spring are modeled here as sets of coupled beams illustrated in Fig. 7. Unlike the thin spring models proposed in [19] and [20], the form given in Eq. (9) reduces

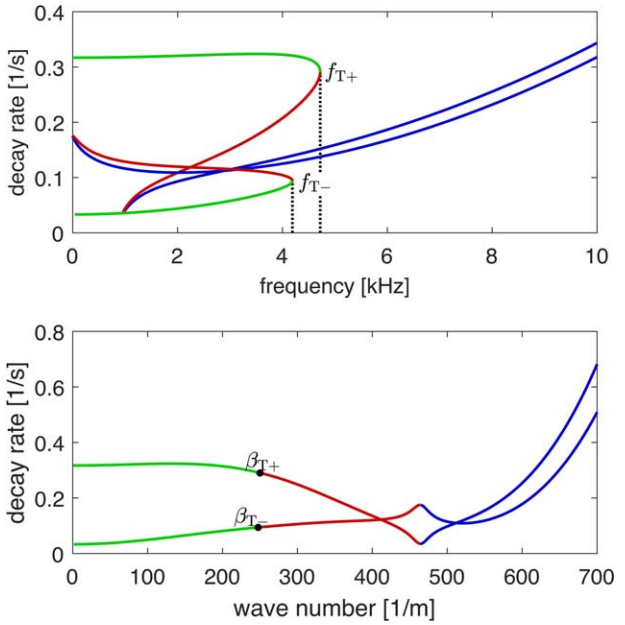


Fig. 6. Decay rate against frequency and wave number for the damped four-variable thin spring model [Eq. (9)] with color coding matching Fig. 5.

to thin beam vibrations [35] in the case of zero curvature (κ = 0) with all coupling terms vanishing [22]:

$$\partial_t^2 u = \frac{-EI}{\rho A}\partial_s^4 u - \left(\sigma_u + \frac{\eta I}{\rho A}\partial_s^4\right)\partial_t u, \tag{15}$$

$$\partial_t^2 v = \frac{-EI}{\rho A}\partial_s^4 v - \left(\sigma_v + \frac{\eta I}{\rho A}\partial_s^4\right)\partial_t v, \tag{16}$$

$$\partial_t^2 w = \frac{E}{\rho}\partial_s^2 w - \left(\sigma_w - \frac{\eta}{\rho}\partial_s^2\right)\partial_t w, \tag{17}$$

$$\partial_t^2 \theta_w = \frac{G}{\rho}\partial_s^2 \theta_w - \left(\sigma_\theta - \frac{\eta}{2\rho(1+\nu)}\partial_s^2\right)\partial_t \theta_w. \tag{18}$$

This allows modeling every component of the full system with the same set of governing equations.

Constructing the full model involves connecting the beam sections to each end of the spring as seen in Fig. 7. In equation form, the nine subsystems are concatenated:

$$\partial_t^2 \tilde{\mathbf{z}} = \tilde{\mathbf{W}}\tilde{\mathbf{z}} - \tilde{\mathbf{\Gamma}}\partial_t \tilde{\mathbf{z}}, \tag{19}$$

$$\tilde{\mathbf{z}} = \begin{bmatrix} u_1 \cdots u_9 & v_1 \cdots v_9 & w_1 \cdots w_9 & \theta_{w1} \cdots \theta_{w9} \end{bmatrix}^\intercal. \tag{20}$$

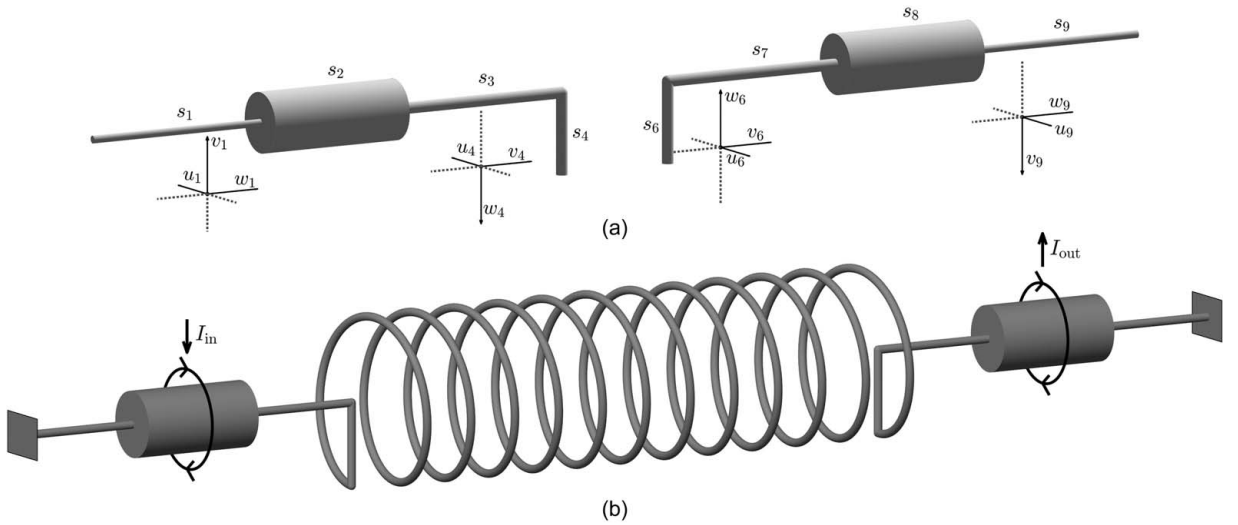


Fig. 7. (a) Magnetic beads and connecting wires modeled as coupled beams. (b) Reverb tank model for a single spring.

The numeric subscript denotes the relevant segment (which now also applies to all parameters describing the material and geometry), and the matrices are built using $\mathbf{W}$ and $\mathbf{\Gamma}$ such that they correspond to $\tilde{\mathbf{z}}$. All subsystems except for the helical spring are evaluated with $\kappa = 0$.

Each connection point requires continuity to be enforced between adjacent subsystems. The coupling between the bead s_2 and support wire s_1 is straightforward with no orientation changes:

$$\begin{aligned} u_{1\mathrm{r}} &= u_{2\mathrm{l}}, & v_{1\mathrm{r}} &= v_{2\mathrm{l}}, & w_{1\mathrm{r}} &= w_{2\mathrm{l}}, \\ \theta_{u1\mathrm{r}} &= \theta_{u2\mathrm{l}}, & \theta_{v1\mathrm{r}} &= \theta_{v2\mathrm{l}}, & \theta_{w1\mathrm{r}} &= \theta_{w2\mathrm{l}}, \\ m_{u1\mathrm{r}} &= m_{u2\mathrm{l}}, & m_{v1\mathrm{r}} &= m_{v2\mathrm{l}}, & m_{w1\mathrm{r}} &= m_{w2\mathrm{l}}, \\ p_{u1\mathrm{r}} &= p_{u2\mathrm{l}}, & p_{v1\mathrm{r}} &= p_{v2\mathrm{l}}, & p_{w1\mathrm{r}} &= p_{w2\mathrm{l}}, \end{aligned} \tag{21}$$

where left and right subscripts are introduced: $u_{1\mathrm{l}} = u_1(0, t)$ and $u_{1\mathrm{r}} = u_1(L_1, t)$. Connections between s_2 and s_3, s_7 and s_8, and s_8 and s_9 follow similarly from Eq. (21). A perpendicular connection is specified between the next support wire s_3 and the *alignment wire* s_4, whose length is set to the spring coil radius R_{c} such that the magnets lie on the spring center-line axis:

$$\begin{aligned} u_{3\mathrm{r}} &= u_{4\mathrm{l}}, & v_{3\mathrm{r}} &= -w_{4\mathrm{l}}, & w_{3\mathrm{r}} &= v_{4\mathrm{l}}, \\ \theta_{u3\mathrm{r}} &= \theta_{u4\mathrm{l}}, & \theta_{v3\mathrm{r}} &= -\theta_{w4\mathrm{l}}, & \theta_{w3\mathrm{r}} &= \theta_{v4\mathrm{l}}, \\ m_{u3\mathrm{r}} &= m_{u4\mathrm{l}}, & m_{v3\mathrm{r}} &= -m_{w4\mathrm{l}}, & m_{w3\mathrm{r}} &= m_{v4\mathrm{l}}, \\ p_{u3\mathrm{r}} &= p_{u4\mathrm{l}}, & p_{v3\mathrm{r}} &= -p_{w4\mathrm{l}}, & p_{w3\mathrm{r}} &= p_{v4\mathrm{l}}, \end{aligned} \tag{22}$$

where the connection between s_6 and s_7 follows accordingly. Finally, continuity at either end of the spring with the alignment wires is mostly perpendicular except for the inclusion of helix angle. Defining $\alpha_{\mathrm{a}} = \cos(\alpha)$ and $\alpha_{\mathrm{b}} = \sin(\alpha)$, the following can be written:

$$\begin{aligned} u_{4\mathrm{r}} &= \alpha_{\mathrm{a}} w_{5\mathrm{l}} - \alpha_{\mathrm{b}} v_{5\mathrm{l}}, & v_{4\mathrm{r}} &= \alpha_{\mathrm{a}} v_{5\mathrm{l}} + \alpha_{\mathrm{b}} w_{5\mathrm{l}}, \\ \theta_{u4\mathrm{r}} &= \alpha_{\mathrm{a}} \theta_{w5\mathrm{l}} - \alpha_{\mathrm{b}} \theta_{v5\mathrm{l}}, & \theta_{v4\mathrm{r}} &= \alpha_{\mathrm{a}} \theta_{v5\mathrm{l}} + \alpha_{\mathrm{b}} \theta_{w5\mathrm{l}}, \\ m_{u4\mathrm{r}} &= \alpha_{\mathrm{a}} m_{w5\mathrm{l}} - \alpha_{\mathrm{b}} m_{v5\mathrm{l}}, & m_{v4\mathrm{r}} &= \alpha_{\mathrm{a}} m_{v5\mathrm{l}} + \alpha_{\mathrm{b}} m_{v5\mathrm{l}}, \\ p_{u4\mathrm{r}} &= \alpha_{\mathrm{a}} p_{w5\mathrm{l}} - \alpha_{\mathrm{b}} p_{v5\mathrm{l}}, & p_{v4\mathrm{r}} &= \alpha_{\mathrm{a}} p_{v5\mathrm{l}} + \alpha_{\mathrm{b}} p_{w5\mathrm{l}}, \\ w_{4\mathrm{r}} &= -u_{5\mathrm{l}}, & \theta_{w4\mathrm{r}} &= -\theta_{u5\mathrm{l}}, \\ m_{w4\mathrm{r}} &= -m_{u5\mathrm{l}}, & p_{w4\mathrm{r}} &= -p_{u5\mathrm{l}}, \end{aligned} \tag{23}$$

and again the connection between s_5 and s_6 follows suit.

2.2.1 Boundary Conditions

Having enforced continuity at all connection points, boundary conditions must be specified only for support wires s_1 and s_9. With the tank design specifying the end wires to be soldered in place externally [4], an appropriate choice is to enforce clamped conditions:

$$\begin{aligned} u_{1\mathrm{l}} &= 0, & \partial_s u_{1\mathrm{l}} &= 0, & u_{9\mathrm{r}} &= 0, & \partial_s u_{9\mathrm{r}} &= 0, \\ v_{1\mathrm{l}} &= 0, & \partial_s v_{1\mathrm{l}} &= 0, & v_{9\mathrm{r}} &= 0, & \partial_s v_{9\mathrm{r}} &= 0, \\ w_{1\mathrm{l}} &= 0, & w_{9\mathrm{r}} &= 0, & \theta_{w1\mathrm{l}} &= 0, & \theta_{w9\mathrm{r}} &= 0. \end{aligned} \tag{24}$$

2.2.2 Energy Analysis

The energy balance of the reverb tank model provides a means of analyzing system passivity, as well as determining boundary and continuity conditions to be lossless. Energy analysis typically involves taking inner products with velocity expressions and applying integration by parts where necessary. For a general introduction to strategies in deriving energy expressions, see [36], from which notation using double vertical bars to denote the accompanying norm of l_2 inner products is borrowed.

First considering the helical spring in isolation, the energy balance for the thin model Eq. (9) (see the Appendix A.1 for the full derivation) is written as

$$\frac{d\mathcal{H}_5}{dt} = \mathcal{B}_5|_{L_5} - \mathcal{B}_5|_0 - \mathcal{Q}_5, \tag{25}$$

where $\mathcal{H}_5$ represents the energy in the spring:

$$\begin{aligned} \mathcal{H}_5 = \frac{\rho_5 A_5}{2} &\left(\|\partial_t u_5\|^2 + \|\partial_t v_5\|^2 + \|\partial_t w_5\|^2\right) \\ &+ \frac{1}{2E_5 I_5}\left(\|m_{u5}\|^2 + \|m_{v5}\|^2\right) + \frac{1}{4G_5 I_5}\left(\|m_{w5}\|^2\right) \\ &+ \rho_5 I_5 \|\partial_t \theta_{w5}\|^2 + \frac{1}{2E_5 A_5}\left(\|p_{w5}\|^2\right), \end{aligned} \tag{26}$$

$\mathcal{B}_5|_{L_5}$ and $\mathcal{B}_5|_0$ are boundary energy terms of the form:

$$\begin{aligned}\mathcal{B}_5 = {} & \partial_t u_5 p_{u5} + \partial_t v_5 p_{v5} + \partial_t w_5 p_{w5} \\ & + \partial_t \theta_{u5} m_{u5} + \partial_t \theta_{v5} m_{v5} + \partial_t \theta_{w5} m_{w5} \\ & + \frac{\eta}{E_5}\Big(\partial_t^2 u_5 p_{u5} + \partial_t^2 v_5 p_{v5} + \partial_t^2 w_5 p_{w5} \\ & + \partial_t^2 \theta_{u5} m_{u5} + \partial_t^2 \theta_{v5} m_{v5} + \partial_t^2 \theta_{w5} m_{w5}\Big),\end{aligned} \tag{27}$$

and $\mathcal{Q}_5$ holds the dissipation terms:

$$\begin{aligned}\mathcal{Q}_5 = {} & \frac{\sigma_u}{2}\|\partial_t u_5\|^2 + \frac{\sigma_v}{2}\|\partial_t v_5\|^2 + \frac{\sigma_w}{2}\|\partial_t w_5\|^2 \\ & + \frac{\eta \rho_5 A_5}{2E_5}\left(\|\partial_t^2 u_5\|^2 + \|\partial_t^2 v_5\|^2 + \|\partial_t^2 w_5\|^2\right) \\ & + \frac{\sigma_\theta}{2}\|\partial_t \theta_{w5}\|^2 + \frac{\eta \rho_5 I_5}{E_5}\|\partial_t^2 \theta_{w5}\|^2.\end{aligned} \tag{28}$$

Lossless boundary conditions must yield $\mathcal{B}_5 = 0$ when evaluated at $s_5 = 0$ and $s_5 = L_5$ in the energy balance Eq. (25). With a view that the upcoming discretization does not consider losses at the boundaries and connection points, Eq. (27) can be evaluated with $\eta = 0$. It is clear that with lossless boundary conditions specified, the model is strictly dissipative thanks to the non-negativity of $\mathcal{Q}_5$ in Eq. (28).

Since each subsystem in the reverb tank model is governed by the same set of equations, the energy balance for the full system is

$$\sum_{n=1}^{9} \frac{d\mathcal{H}_n}{dt} = \sum_{n=1}^{9} \left(\mathcal{B}_n|_{L_n} - \mathcal{B}_n|_0 - \mathcal{Q}_n\right), \tag{29}$$

where the summation of dissipation terms is still always non-negative. The outer boundary energy expressions $\mathcal{B}_1|_0$ and $\mathcal{B}_9|_{L_9}$ are zero for the clamped conditions specified in Eq. (24), which are lossless for beams [36]. Substituting continuity conditions from Eqs. (21)–(23) and those for coupling points that follow suit into Eq. (29) cancels all remaining boundary energy terms in pairs (e.g., $\mathcal{B}_1|_{L_1} - \mathcal{B}_2|_0 = 0$. As such, all continuity conditions specified are lossless: energy can flow between adjacent subsystems but cannot change at the coupling points.

2.2.3 Input and Output

In determining how a supply current I_{in} relates to the torque driving a magnetic bead, design specifications in [2] based on the simplifying assumption of unidirectional coupling state that supplying an alternating current of constant magnitude with increasing frequency results in constant velocity driving of the bead. Taking into consideration that this simplified model aligns with experimental observation in [23], it is adopted here. From Newton's second law, driving the bead with a torque would result in constant acceleration. As such, supplying a torque that results in constant velocity requires a differentiated input:

$$T_{\text{in}} = \chi_{\text{in}} \frac{d}{dt} I_{\text{in}}, \tag{30}$$

which holds under the assumption that no other forces act on the bead. The scaling factor χ_{in} accounts for the mapping between T_{in} and $\frac{d}{dt} I_{\text{in}}$ due to the magnetic field induced by the current.

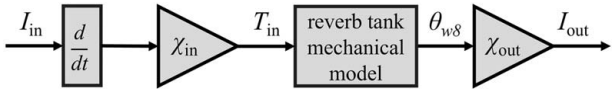


Fig. 8. Driving and pick-up configuration in the reverb tank model.

At the pick-up transducer, a change in magnetic flux will induce an electromotive force in the coil of wire around the metal laminations [3]. The change in flux correlates directly to the bead rotating, meaning an output voltage is induced corresponding to the velocity of the bead. Given that the voltage and current are related through an inductance $\mathcal{L}$ for a coil of wire: $I_{\text{out}} = \frac{1}{\mathcal{L}} \int V_{\text{out}}\, dt$, the output current can be stated as

$$I_{\text{out}} = \chi_{\text{out}} \theta_{w8}. \tag{31}$$

Fig. 8 schematically depicts this driving and pick-up configuration. For simplicity, the constants χ_{in} and χ_{out} are omitted and accounted for with an empirically determined overall scaling factor for comparison to measurement.

Given the linearity of the reverb tank model, the differentiation required at the input can be more conveniently incorporated at the output, now reading angular velocity $\partial_t \theta_{w8}$ instead of displacement. As such, the input and output is specified for the model equations in Eq. (19) as

$$\partial_t^2 \tilde{\mathbf{z}} = \tilde{\mathbf{W}}\tilde{\mathbf{z}} - \tilde{\mathbf{\Gamma}}\partial_t \tilde{\mathbf{z}} + \mathbf{k}_{\text{in}} I_{\text{in}}, \quad I_{\text{out}} = \int_0^{\tilde{L}} \mathbf{k}_{\text{out}} \partial_t \tilde{\mathbf{z}}\, \mathrm{d}\tilde{s}, \tag{32}$$

over the domain $\tilde{s} \in [0 \quad \tilde{L}]$ defined using the total system length $\tilde{L} = \sum_{n=1}^{9} L_n$. Input and output vectors are defined as

$$\mathbf{k}_{\text{in}} = [0 \quad 0 \quad 0 \quad \psi_{\text{in}}(\tilde{s})]^{\mathsf{T}}, \quad \mathbf{k}_{\text{out}} = [0 \quad 0 \quad 0 \quad \psi_{\text{out}}(\tilde{s})], \tag{33}$$

using the distributions

$$\psi_{\text{in}}(\tilde{s}) = \begin{cases} \frac{1}{L_2} & : \quad L_1 < \tilde{s} < (L_1 + L_2) \\ 0 & : \quad \text{otherwise} \end{cases}, \tag{34}$$

$$\psi_{\text{out}}(\tilde{s}) = \begin{cases} \frac{1}{L_8} & : \quad \sum_{n=1}^{7} L_n < \tilde{s} < \sum_{n=1}^{8} L_n \\ 0 & : \quad \text{otherwise} \end{cases}. \tag{35}$$

The model is set up with this driving because reverb tanks typically employ a constant current source for audio applications [2], but the measured impulse response in Fig. 1 uses a constant voltage driving signal. Recalling that $I_{\text{in}} = \frac{1}{\mathcal{L}} \int V_{\text{in}}\, dt$ for a coil of wire, this would be accounted for by integrating the driving current. As such, Fig. 8 with the differentiation removed represents the driving/pick-up of the model for a constant voltage source.

3 SOLVING IN SPACE: CHEBYSHEV PSEUDOSPECTRAL METHOD

Broadly speaking, spectral methods provide a means to find the numerical solution of a differential equation; see [37–39] for comprehensive introductions on this topic. An underlying assumption of the method is that the spatial

solution of a problem can be approximated with $M+1$ basis functions. First-kind Chebyshev polynomials are employed here:

$$T_m(s) = \cos\left(m \cos^{-1}(s)\right). \tag{36}$$

With this basis, the following can be written:

$$u(s,t) = \sum_{m=0}^{M} \hat{u}_m(t)\, T_m(s), \tag{37}$$

where $\hat{u}_m$ represents a set of series coefficients. Different approaches within spectral methods mainly vary on their strategy of determining $\hat{u}_m$ to minimize error. The pseudospectral method is chosen here for its versatility, in particular its ability to handle any set of end conditions. This involves setting the residual (error measure) to zero at a set of collocation points and these are typically specified with nonuniform grid spacing clustering points near boundaries to avoid error introduced by the Runge phenomenon [37].

A Gauss-Chebyshev-Lobatto grid is chosen in this application:

$$s_j = \left(\frac{-s_j^\star + 1}{2}\right) L, \quad s_j^\star = \cos\left(\frac{j\pi}{M}\right), \tag{38}$$

where $j = 0, 1 \ldots M$, which is derived by evaluating the extrema of first-kind Chebyshev polynomials. Since the pseudospectral approach aims to find the spatial solution over a finite set of points, nth-order differentiation is represented with a matrix $\mathbf{D}^n$, which can be generated using the MATLAB function `diffmat.m` available with Chebfun [40, 41].

The motivation for this discretization approach lies with the global nature of approximations. This allows the use of a high-order approximation for each subsystem without the need to eliminate *ghost nodes*, which are necessary for local discretization methods such as finite difference schemes and trivial only for specific boundary conditions such as those imposed in [13] and [21] in simplified modeling of a spring reverb tank.

3.1 Semi-Discrete Model

Building grid points for each subsystem and transforming the matrices $\tilde{\mathbf{W}}$ and $\tilde{\mathbf{\Gamma}}$ by replacing spatial derivative operators with nth-order differentiation matrices $\mathbf{D}^n$, the reverb tank model Eq. (32) is spatially discretized as

$$\frac{d^2}{dt^2}\overline{\mathbf{z}} = \overline{\mathbf{W}}\overline{\mathbf{z}} - \overline{\mathbf{\Gamma}}\frac{d}{dt}\overline{\mathbf{z}} + \overline{\mathbf{k}}_{\text{in}} I_{\text{in}}, \quad I_{\text{out}} = \overline{\mathbf{k}}_{\text{out}}\frac{d}{dt}\overline{\mathbf{z}}, \tag{39}$$

where

$$\overline{\mathbf{z}} = [\mathbf{u}_1^\mathsf{T} \cdots \mathbf{u}_9^\mathsf{T}\ \mathbf{v}_1^\mathsf{T} \cdots \mathbf{v}_9^\mathsf{T}\ \mathbf{w}_1^\mathsf{T} \cdots \mathbf{w}_9^\mathsf{T}\ \ \boldsymbol{\theta}_{w1}^\mathsf{T} \cdots \boldsymbol{\theta}_{w9}^\mathsf{T}]^\mathsf{T}, \tag{40}$$

with vectors in $\overline{\mathbf{z}}$ defined by indexing displacement variables on a Gauss-Chebyshev-Lobatto grid, for example,

$$\mathbf{u}_1 = [u_1(s_{1,0}, t) \quad u_1(s_{1,1}, t) \cdots u_1(s_{1,M_1}, t)]^\mathsf{T}. \tag{41}$$

Input and output vectors $\overline{\mathbf{k}}_{\text{in}}$ and $\overline{\mathbf{k}}_{\text{out}}$ hold the distribution functions in Eqs. (34) and (35) sampled on the full domain grid $\tilde{\mathbf{s}}$:

$$\overline{\mathbf{k}}_{\text{in}} = \left[\mathbf{0}\ \mathbf{0}\ \mathbf{0}\ \ \boldsymbol{\xi}_{\text{in}}\ \boldsymbol{\psi}_{\text{in}}\right]^\mathsf{T},\ \overline{\mathbf{k}}_{\text{out}} = \left[\mathbf{0} \quad \mathbf{0} \quad \mathbf{0} \quad \boldsymbol{\xi}_{\text{out}}\ \boldsymbol{\psi}_{\text{out}}\right], \tag{42}$$

$$\tilde{\mathbf{s}} = \left[\mathbf{s}_1^\mathsf{T} \cdots \mathbf{s}_9^\mathsf{T}\right], \tag{43}$$

where the null row vector $\mathbf{0}$ is the same length as $\tilde{\mathbf{s}}$. The new weight vectors $\boldsymbol{\xi}_{\text{in}}$ and $\boldsymbol{\xi}_{\text{out}}$ are defined over the full system length $\tilde{L}$ as

$$\boldsymbol{\xi}_{\text{in}} = \begin{cases} \boldsymbol{\xi}_2 & : \quad L_1 < \tilde{\mathbf{s}} < (L_1 + L_2) \\ 0 & : \quad \text{otherwise} \end{cases}, \tag{44}$$

$$\boldsymbol{\xi}_{\text{out}} = \begin{cases} \boldsymbol{\xi}_8 & : \quad \sum_{n=1}^{7} L_n < \tilde{\mathbf{s}} < \sum_{n=1}^{8} L_n \\ 0 & : \quad \text{otherwise} \end{cases}, \tag{45}$$

where

$$\xi_{2,j} = \sin(j\pi/M_2), \quad \xi_{8,j} = \sin(j\pi/M_8), \tag{46}$$

and account for the grid spacing such that excitation/pick-up over the magnetic beads remains spatially uniform [37]. For practical purposes, $N = M + 1$ is specified such that now $j = 1, 2 \ldots N$, where N is the number of grid points.

3.2 Boundary Bordering

The boundary bordering procedure is applied to enforce both the boundary and continuity conditions and involves replacing collocation points with numerical versions of end conditions: this is realized as row replacement in the system matrices [37]. As such, the boundary conditions in Eq. (24) become

$$\begin{aligned}
\left[1 \cdots 0 \quad\right]\mathbf{u}_1 = 0, &\quad \mathbf{d}_1^1 \mathbf{u}_1 = 0, \\
\left[0 \cdots 1\right]\mathbf{u}_9 = 0, &\quad \mathbf{d}_N^1 \mathbf{u}_9 = 0, \\
\left[1 \cdots 0\right]\mathbf{v}_1 = 0, &\quad \mathbf{d}_1^1 \mathbf{v}_1 = 0, \\
\left[0 \cdots 1\right]\mathbf{v}_9 = 0, &\quad \mathbf{d}_N^1 \mathbf{v}_9 = 0, \\
\left[1 \cdots 0\right]\mathbf{w}_1 = 0, &\quad \left[0 \cdots 1\right]\mathbf{w}_9 = 0, \\
\left[1 \cdots 0\right]\boldsymbol{\theta}_{w1} = 0, &\quad \left[0 \cdots 1\right]\boldsymbol{\theta}_{w9} = 0,
\end{aligned} \tag{47}$$

where $\mathbf{d}_p^n$ represents the pth row of an nth-order differentiation matrix and the other premultiplying vectors hold only one nonzero element. Continuity conditions are implemented following the same procedure.

3.3 Eigenvalue Problem

Following row replacement enforcing the boundary and continuity conditions, grouping the vector/matrix elements corresponding to those representing boundaries (subscript B) and interior collocation points (subscript I) gives

$$\begin{aligned}
\begin{bmatrix} \mathbf{0} \\ \frac{d^2}{dt^2}\overline{\mathbf{z}}_{\text{I}} \end{bmatrix} &= \begin{bmatrix} \overline{\mathbf{W}}_{\text{BB}} & \overline{\mathbf{W}}_{\text{BI}} \\ \overline{\mathbf{W}}_{\text{IB}} & \overline{\mathbf{W}}_{\text{II}} \end{bmatrix} \begin{bmatrix} \overline{\mathbf{z}}_{\text{B}} \\ \overline{\mathbf{z}}_{\text{I}} \end{bmatrix} \\
&\quad - \begin{bmatrix} \overline{\mathbf{\Gamma}}_{\text{BB}} & \overline{\mathbf{\Gamma}}_{\text{BI}} \\ \overline{\mathbf{\Gamma}}_{\text{IB}} & \overline{\mathbf{\Gamma}}_{\text{II}} \end{bmatrix} \frac{d}{dt} \begin{bmatrix} \overline{\mathbf{z}}_{\text{B}} \\ \overline{\mathbf{z}}_{\text{I}} \end{bmatrix} + \begin{bmatrix} \overline{\mathbf{k}}_{\text{in,B}} \\ \overline{\mathbf{k}}_{\text{in,I}} \end{bmatrix} I_{\text{in}},
\end{aligned} \tag{48}$$

$$I_{\text{out}} = \begin{bmatrix} \overline{\mathbf{k}}_{\text{out,B}} & \overline{\mathbf{k}}_{\text{out,I}} \end{bmatrix} \frac{d}{dt} \begin{bmatrix} \overline{\mathbf{z}}_{\text{B}} \\ \overline{\mathbf{z}}_{\text{I}} \end{bmatrix}. \tag{49}$$

Since the vectors $\boldsymbol{\xi}_{\text{in}}$ and $\boldsymbol{\xi}_{\text{out}}$ in Eq. (42) are introduced to ensure the driving/pick-up is spatially uniform, $\overline{\mathbf{k}}_{\text{in,B}}$ and

$\overline{\mathbf{k}}_{\text{out,B}}$ by definition have no nonzero elements. In addition, losses have not been included at the boundaries and connection points, meaning $\overline{\mathbf{\Gamma}}_{\text{BB}}$ and $\overline{\mathbf{\Gamma}}_{\text{BI}}$ are both null matrices. Thus, the first row of the rearranged eigenvalue problem Eq. (48) can be written as

$$\mathbf{0} = \overline{\mathbf{W}}_{\text{BB}}\overline{\mathbf{z}}_{\text{B}} + \overline{\mathbf{W}}_{\text{BI}}\overline{\mathbf{z}}_{\text{I}}, \tag{50}$$

$$\overline{\mathbf{z}}_{\text{B}} = -\overline{\mathbf{W}}_{\text{BB}}^{-1}\overline{\mathbf{W}}_{\text{BI}}\overline{\mathbf{z}}_{\text{I}}, \tag{51}$$

$$\frac{d}{dt}\overline{\mathbf{z}}_{\text{B}} = -\overline{\mathbf{W}}_{\text{BB}}^{-1}\overline{\mathbf{W}}_{\text{BI}}\frac{d}{dt}\overline{\mathbf{z}}_{\text{I}}, \tag{52}$$

and the second row gives

$$\frac{d^2}{dt^2}\overline{\mathbf{z}}_{\text{I}} = \overline{\mathbf{W}}_{\text{IB}}\overline{\mathbf{z}}_{\text{B}} + \overline{\mathbf{W}}_{\text{II}}\overline{\mathbf{z}}_{\text{I}} - \overline{\mathbf{\Gamma}}_{\text{IB}}\frac{d}{dt}\overline{\mathbf{z}}_{\text{B}} - \overline{\mathbf{\Gamma}}_{\text{II}}\frac{d}{dt}\overline{\mathbf{z}}_{\text{I}} + \overline{\mathbf{k}}_{\text{in,I}}I_{\text{in}}. \tag{53}$$

Substituting the boundary expressions Eqs. (51) and (52) into the equation for interior collocation points, Eq. (53) yields

$$\frac{d^2}{dt^2}\overline{\mathbf{z}}_{\text{I}} = \mathbf{Z}_{\mathbf{W}}\overline{\mathbf{z}}_{\text{I}} + \mathbf{Z}_{\mathbf{\Gamma}}\frac{d}{dt}\overline{\mathbf{z}}_{\text{I}} + \overline{\mathbf{k}}_{\text{in,I}}I_{\text{in}}, \tag{54}$$

where

$$\mathbf{Z}_{\mathbf{W}} = -\overline{\mathbf{W}}_{\text{IB}}\overline{\mathbf{W}}_{\text{BB}}^{-1}\overline{\mathbf{W}}_{\text{BI}} + \overline{\mathbf{W}}_{\text{II}},$$
$$\mathbf{Z}_{\mathbf{\Gamma}} = \overline{\mathbf{\Gamma}}_{\text{IB}}\overline{\mathbf{W}}_{\text{BB}}^{-1}\overline{\mathbf{W}}_{\text{BI}} - \overline{\mathbf{\Gamma}}_{\text{II}}, \tag{55}$$

and the output is written as

$$I_{\text{out}} = \overline{\mathbf{k}}_{\text{out,I}}\frac{d}{dt}\overline{\mathbf{z}}_{\text{I}}. \tag{56}$$

4 MODAL FORMULATION

4.1 State-Space Representation

Since matrices $\mathbf{Z}_{\mathbf{W}}$ and $\mathbf{Z}_{\mathbf{\Gamma}}$ in the eigenvalue problem Eq. (54) are not simultaneously diagonalizable (as they would be, e.g., for a proportionally damped system), the system is rewritten in first-order form [42]:

$$\frac{d}{dt}\boldsymbol{\zeta} = \overline{\mathbf{A}}\boldsymbol{\zeta} + \overline{\mathbf{b}}I_{\text{in}}, \quad I_{\text{out}} = \overline{\mathbf{c}}\,\boldsymbol{\zeta}, \tag{57}$$

where

$$\boldsymbol{\zeta} = \begin{bmatrix}\overline{\mathbf{z}}_{\text{I}} \\ \frac{d}{dt}\overline{\mathbf{z}}_{\text{I}}\end{bmatrix}, \ \overline{\mathbf{A}} = \begin{bmatrix}\mathbf{0} & \mathbf{I} \\ \mathbf{Z}_{\mathbf{W}} & \mathbf{Z}_{\mathbf{\Gamma}}\end{bmatrix},$$
$$\overline{\mathbf{b}} = \begin{bmatrix}\mathbf{0} \\ \overline{\mathbf{k}}_{\text{in,I}}\end{bmatrix}, \quad \overline{\mathbf{c}} = \begin{bmatrix}\mathbf{0} & \overline{\mathbf{k}}_{\text{out,I}}\end{bmatrix}. \tag{58}$$

4.2 Diagonalization

The state-space model is transformed to its modal canonical form by diagonalizing $\overline{\mathbf{A}} = \overline{\mathbf{\Lambda}}\,\overline{\mathbf{\Omega}}\,\overline{\mathbf{\Lambda}}^{-1}$, premultiplying with $\overline{\mathbf{\Lambda}}^{-1}$, and letting $\overline{\boldsymbol{\zeta}} = \overline{\mathbf{\Lambda}}^{-1}\boldsymbol{\zeta}$:

$$\frac{d}{dt}\overline{\boldsymbol{\zeta}} = \overline{\mathbf{\Omega}}\,\overline{\boldsymbol{\zeta}} + \overline{\mathbf{\Lambda}}^{-1}\overline{\mathbf{b}}I_{\text{in}}, \quad I_{\text{out}} = \overline{\mathbf{c}}\,\overline{\mathbf{\Lambda}}\,\overline{\boldsymbol{\zeta}}. \tag{59}$$

The elements of diagonal matrix $\overline{\mathbf{\Omega}}$ are the system eigenvalues λ_i and appear as complex conjugate pairs, with decay rate $\tilde{\alpha}_i = -\text{Re}(\lambda_i)$ and resonance frequency $\omega_{\text{r},\,i} = \text{Im}(\lambda_i)$, using i to denote the mode index. The system in Eq. (59) can be said to hold complex modes [42, 43], and a real-valued representation can be written in block-diagonal form. New eigenvalue and eigenvector matrices $\tilde{\mathbf{\Omega}}$ and $\tilde{\mathbf{\Lambda}}$ are derived by reordering $\overline{\mathbf{\Omega}}$ and $\overline{\mathbf{\Lambda}}$, where each mode in $\tilde{\mathbf{\Omega}}$ is a two-by-two block.[1] Writing the system Eq. (59) for a single mode, now using $\tilde{\mathbf{\Omega}}$ and $\tilde{\mathbf{\Lambda}}$, and letting $\tilde{\boldsymbol{\zeta}} = \tilde{\mathbf{\Lambda}}^{-1}\boldsymbol{\zeta}$ (akin to $\overline{\boldsymbol{\zeta}}$) yields

$$\frac{d}{dt}\underbrace{\begin{bmatrix}p_i \\ q_i\end{bmatrix}}_{\tilde{\boldsymbol{\zeta}}_i} = \underbrace{\begin{bmatrix}-\tilde{\alpha}_i & \omega_{\text{r},i} \\ -\omega_{\text{r},i} & -\tilde{\alpha}_i\end{bmatrix}}_{\tilde{\mathbf{\Omega}}_{i,i}}\begin{bmatrix}p_i \\ q_i\end{bmatrix} + \underbrace{\begin{bmatrix}c_{\text{in,p},i} \\ c_{\text{in,q},i}\end{bmatrix}}_{\mathbf{c}_{\text{in},i}}I_{\text{in}},$$
$$I_{\text{out},i} = \underbrace{\begin{bmatrix}c_{\text{out,p},i} & c_{\text{out,q},i}\end{bmatrix}}_{\mathbf{c}_{\text{out},i}}\begin{bmatrix}p_i \\ q_i\end{bmatrix}, \tag{60}$$

where $\mathbf{c}_{\text{in}} = \tilde{\mathbf{\Lambda}}^{-1}\overline{\mathbf{b}}$ and $\mathbf{c}_{\text{out}} = \overline{\mathbf{c}}\,\tilde{\mathbf{\Lambda}}$ denote the input and output mode amplitudes, respectively. The second-order representation of Eq. (60) differs from the usual form (as in [13, 21, 22]) in that it incorporates a phase offset, as shown in the Appendix A.2.

4.3 Time Discretization

To exactly preserve the resonance frequency, decay rate, amplitude, and phase offset of each modal oscillator, the impulse invariant method will be employed, which requires an expression for the oscillator impulse response [44]. First, writing the real-valued form for each complex mode in Eq. (60) as separate equations gives

$$\frac{d}{dt}p_i = -\tilde{\alpha}_i\,p_i + \omega_{\text{r},i}\,q_i + c_{\text{in,p},i}\,I_{\text{in}}, \tag{61}$$

$$\frac{d}{dt}q_i = -\omega_{\text{r},i}\,p_i - \tilde{\alpha}_i\,q_i + c_{\text{in,q},i}\,I_{\text{in}}, \tag{62}$$

$$I_{\text{out},i} = c_{\text{out,p},i}\,p_i + c_{\text{out,q},i}\,q_i. \tag{63}$$

Dropping the i subscript for convenience and taking the Laplace transform, the following is obtained:

$$\hat{s}\,P = -\tilde{\alpha}\,P + \omega_{\text{r}}\,Q + c_{\text{in,p}}\hat{I}_{\text{in}}, \tag{64}$$

$$\hat{s}\,Q = -\omega_{\text{r}}\,P - \tilde{\alpha}\,Q + c_{\text{in,q}}\hat{I}_{\text{in}}, \tag{65}$$

$$\hat{I}_{\text{out}} = c_{\text{out,p}}\,P + c_{\text{out,q}}\,Q, \tag{66}$$

where $\hat{s} = \text{j}\omega$, $\hat{I}_{\text{in}} = \hat{I}_{\text{in}}(\hat{s})$ and $\hat{I}_{\text{out}} = \hat{I}_{\text{out}}(\hat{s})$. In this form, P and Q can be expressed separately in terms of $\hat{I}_{\text{in}}$:

$$P = \frac{\omega_{\text{r}}c_{\text{in,q}} + (\hat{s} + \tilde{\alpha})\,c_{\text{in,p}}}{(\hat{s} + \tilde{\alpha})^2 + \omega_{\text{r}}^2}\hat{I}_{\text{in}}, \tag{67}$$

$$Q = \frac{-\omega_{\text{r}}c_{\text{in,p}} + (\hat{s} + \tilde{\alpha})\,c_{\text{in,q}}}{(\hat{s} + \tilde{\alpha})^2 + \omega_{\text{r}}^2}\hat{I}_{\text{in}}, \tag{68}$$

meaning the transfer function can be written as

$$H(\hat{s}) = \frac{\hat{I}_{\text{out}}}{\hat{I}_{\text{in}}} = \frac{c_{\text{out,p}}P + c_{\text{out,q}}Q}{\hat{I}_{\text{in}}}, \tag{69}$$

and applying the inverse Laplace transform separately to $H_{\text{P}} = P/\hat{I}_{\text{in}}$ and $H_{\text{Q}} = Q/\hat{I}_{\text{in}}$ yields impulse response ex-

[1] In MATLAB, the function `cdf2rdf()` transforms matrices such that eigenvalues are stored in real block diagonal form.

pressions:

$$h_{\mathrm{p}}(t) = C_{1\mathrm{p}}\mathrm{e}^{(\mathrm{j}\omega_{\mathrm{r}}-\tilde{\alpha})t} + C_{2\mathrm{p}}\mathrm{e}^{(-\mathrm{j}\omega_{\mathrm{r}}-\tilde{\alpha})t},$$
$$C_{1\mathrm{p}} = \frac{c_{\mathrm{in,p}} - \mathrm{j}c_{\mathrm{in,q}}}{2}, \quad C_{2\mathrm{p}} = \frac{c_{\mathrm{in,p}} + \mathrm{j}c_{\mathrm{in,q}}}{2}, \tag{70}$$

$$h_{\mathrm{q}}(t) = C_{1\mathrm{q}}\mathrm{e}^{(\mathrm{j}\omega_{\mathrm{r}}-\tilde{\alpha})t} + C_{2\mathrm{q}}\mathrm{e}^{(-\mathrm{j}\omega_{\mathrm{r}}-\tilde{\alpha})t},$$
$$C_{1\mathrm{q}} = \frac{c_{\mathrm{in,q}} + \mathrm{j}c_{\mathrm{in,p}}}{2}, \quad C_{2\mathrm{q}} = \frac{c_{\mathrm{in,q}} - \mathrm{j}c_{\mathrm{in,p}}}{2}. \tag{71}$$

These can then be written in discrete time by introducing a sampling frequency f_{s} and corresponding time step $\Delta_t = 1/f_{\mathrm{s}}$:

$$h_{\mathrm{p}}(n\Delta_t) = C_{1\mathrm{p}}\mathrm{e}^{(\mathrm{j}\omega_{\mathrm{r}}-\tilde{\alpha})n\Delta_t} + C_{2\mathrm{p}}\mathrm{e}^{(-\mathrm{j}\omega_{\mathrm{r}}-\tilde{\alpha})n\Delta_t}, \tag{72}$$

$$h_{\mathrm{q}}(n\Delta_t) = C_{1\mathrm{q}}\mathrm{e}^{(\mathrm{j}\omega_{\mathrm{r}}-\tilde{\alpha})n\Delta_t} + C_{2\mathrm{q}}\mathrm{e}^{(-\mathrm{j}\omega_{\mathrm{r}}-\tilde{\alpha})n\Delta_t}, \tag{73}$$

where n is the sample index. Finally, digital transfer functions are obtained after applying a z-transform and using the geometric series [44]:

$$H_{\mathrm{p}}(z) = \frac{b_{0\mathrm{p}} + b_{1\mathrm{p}}z^{-1}}{1 + a_1 z^{-1} + a_2 z^{-2}}, \tag{74}$$

$$H_{\mathrm{q}}(z) = \frac{b_{0\mathrm{q}} + b_{1\mathrm{q}}z^{-1}}{1 + a_1 z^{-1} + a_2 z^{-2}}, \tag{75}$$

where

$$b_{0\mathrm{p}} = \Delta_t c_{\mathrm{in,p}}, \quad b_{0\mathrm{q}} = \Delta_t c_{\mathrm{in,q}},$$
$$b_{1\mathrm{p}} = \Delta_t \mathrm{e}^{-\tilde{\alpha}\Delta_t}\Big[c_{\mathrm{in,q}}\sin(\omega_{\mathrm{r}}\Delta_t) - c_{\mathrm{in,p}}\cos(\omega_{\mathrm{r}}\Delta_t)\Big],$$
$$b_{1\mathrm{q}} = -\Delta_t \mathrm{e}^{-\tilde{\alpha}\Delta_t}\Big[c_{\mathrm{in,p}}\sin(\omega_{\mathrm{r}}\Delta_t) + c_{\mathrm{in,q}}\cos(\omega_{\mathrm{r}}\Delta_t)\Big],$$
$$a_1 = -2\mathrm{e}^{-\tilde{\alpha}}\Delta_t\cos(\omega_{\mathrm{r}}\Delta_t), \quad a_2 = \mathrm{e}^{-2\tilde{\alpha}\Delta_t}, \tag{76}$$

which also incorporates scaling by Δ_t to account for the difference between the Dirac delta and the Kronecker delta.

4.4 Modal Engine

Modal update equations are built directly from the digital transfer functions Eqs. (74) and (75) for any selection of $\tilde{N}$ modes:

$$p_i^{n+1} = b_{0\mathrm{p},i}\, I_{\mathrm{in}}^{n+1} + b_{1\mathrm{p},i}\, I_{\mathrm{in}}^{n} - a_{1,i}\, p_i^{n} - a_{2,i}\, p_i^{n-1}, \tag{77}$$

$$q_i^{n+1} = b_{0\mathrm{q},i}\, I_{\mathrm{in}}^{n+1} + b_{1\mathrm{q},i}\, I_{\mathrm{in}}^{n} - a_{1,i}\, q_i^{n} - a_{2,i}\, q_i^{n-1}, \tag{78}$$

$$I_{\mathrm{out}}^{n} = \sum_{i=1}^{\tilde{N}} c_{\mathrm{out,p},i}\, p_i^{n} + c_{\mathrm{out,q},i}\, q_i^{n}. \tag{79}$$

While it would be doubly efficient to derive one update equation from $H(\hat{s})$, direct discretization of p and q is necessary for model visualization because they form $\tilde{\boldsymbol{\xi}}_i$ in Eq. (60), which is required for recovering displacement and velocity across the system: $\boldsymbol{\zeta} = \tilde{\boldsymbol{\Lambda}}\tilde{\boldsymbol{\xi}}$. An animation of the system vibrations in response to impulsive excitation is available online,[2] with parameters from the reverb unit in an Olson X-82 amplifier [6]. This unit is chosen because the shorter spring compared to those in the tank in Fig. 3 allows better legibility. The visualization demonstrates how the dominant travelling wave corresponds to global rotation of the spring (i.e., the polarization that best couples with bead rotation), which is in agreement with discussions around the dispersion relation in SEC. 2.1.1. The animation also exemplifies the high degree of dispersion, directly visualizing how the initial impulse "spreads" as it travels along the spring.

5 RESULTS AND MODEL EVALUATION

The model impulse response is computed at audio sample rate $f_{\mathrm{s}} = 48$ kHz for each spring in the tank from Fig. 3 with parameters given in Table 1. The end support wires are made of a beryllium copper alloy, the magnetic beads are a ceramic magnetic material, and the remaining wires and the spring are steel [4]. Damping parameters are set empirically and use the same values for all subsystems. MATLAB code and sound examples are available online.[3]

The eigenvalue problem is computed separately for each spring with $N = 30$ for all beam components, $N = 1{,}450$ for each polarization of spring 1, and $N = 1{,}750$ for spring 2, capturing vibrations up to around 13 and 14 kHz, respectively. Only modes up to 12 kHz are retained after diagonalization, which is reasonable considering the lower energy at high frequencies in measured impulse responses, leaving 3,835 damped modes: 1,752 for spring 1 and 2,083 for spring 2. The authors' practical observations are that this inherently removes spurious modes, including modes with negative damping. Spurious modes are difficult to avoid with the pseudospectral method, in particular when boundary bordering is applied [45], and typically have large eigenvalues (i.e., high mode frequencies).

With the reverb tank model set up for constant current driving typical for audio applications, the input/output must be adjusted to account for the constant voltage driving employed in the impulse response measurement. As discussed in SEC. 2.2.3, differentiating the input signal is no longer required and this is accounted for at the output, reading displacement instead of velocity. The state-space representation in Eq. (57) makes this change convenient, with the output distribution vector in Eq. (58) becoming $\bar{\mathbf{c}} = \begin{bmatrix}\bar{\mathbf{k}}_{\mathrm{out,I}} & \mathbf{0}\end{bmatrix}$.

As a baseline, Fig. 9 compares an impulse response generated by the thin spring model with no magnetic beads to the measurement in Fig. 1 both in spectrogram form and in the time domain. The latter offsets each output for visual comparison. The simplified boundary conditions, input and output defined at each end of the spring, and decay rates set directly for the modal oscillators are taken from [22], with related studies seeing similar outputs [20, 21]. With no magnetic beads, discrepancies are mostly due to incorrect mode amplitudes—even with accurate modeling of helical spring vibrations in the hearing range, the match with measurement is poor.

[2] https://youtu.be/X_3GsgH4iYE?si=KY3KHqSyJvcKKLsq.

[3] https://github.com/jacobmcquillan/physical-modelling-of-a-spring-reverb-tank.

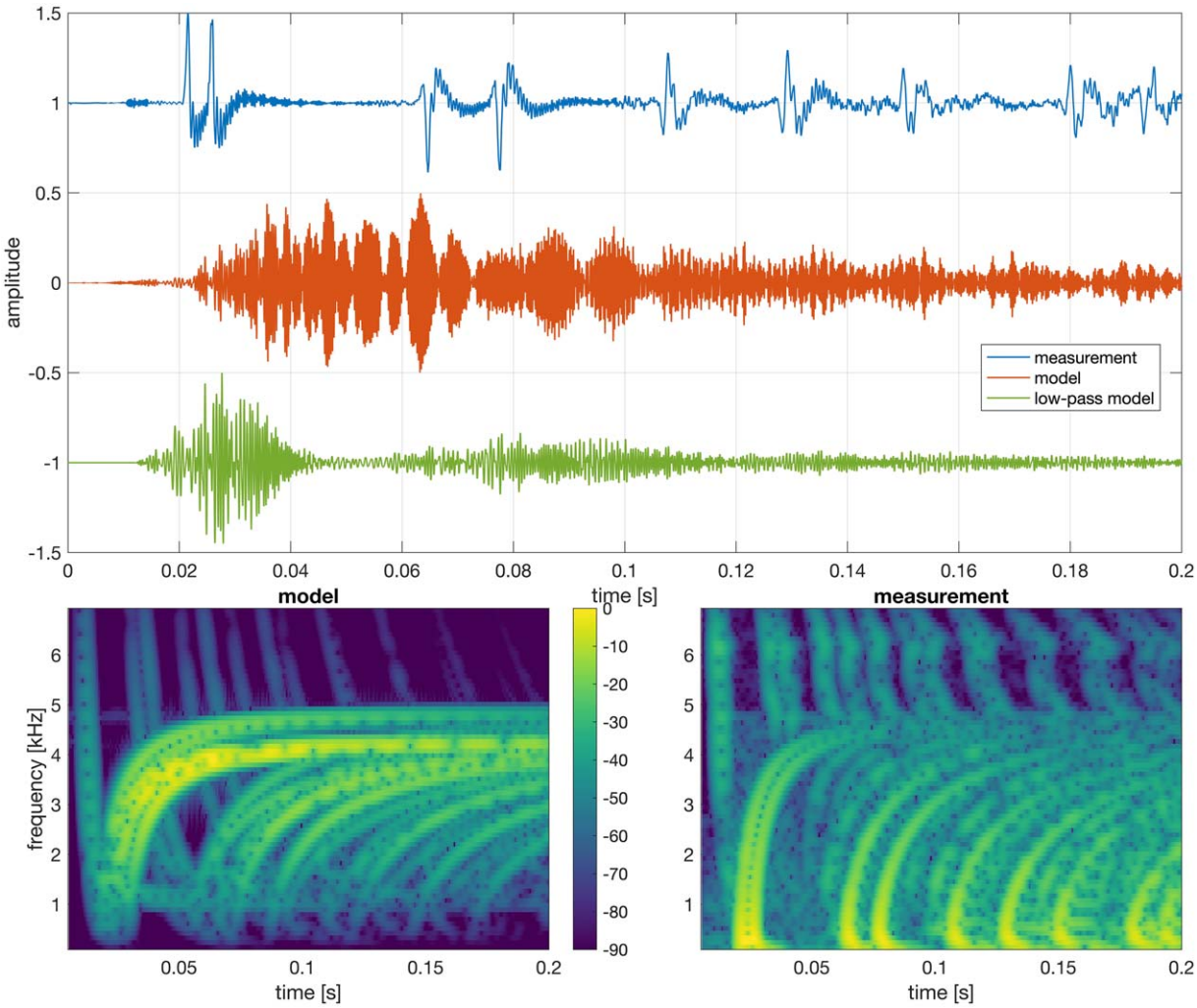


Fig. 9. Impulse response comparison of a thin spring model with no magnetic beads and a measured spring reverb tank.

Fig. 10 compares the simulated tank impulse response to the measurement in the same format as the baseline in Fig. 9. The results show the main features of the measured response are reproduced including the shape of the main chirps (notably how they bend at low frequencies and taper off at the transition frequency), the echo density at both low and high frequencies, the blurring of reflections over time, and the various sets of secondary chirps. It is worth noting that the transition frequencies are a little mismatched: this reflects the compromise struck in fine-tuning the echo density for the time domain comparison using the Young's modulus. There are also some discrepancies in the comparison, the most significant visible in the overall response above the transition frequency. Below the transition frequency, the secondary chirps appear more faint in the model than in the measurement.

A second comparison is presented using the same reverb tank for the response of a single bead-spring-bead system shown over a longer response time. Fig. 11 again compares impulse response spectrograms, now supplemented with frequency domain representations to further inspect the aforementioned discrepancies. These likely stem from modeling simplifications (e.g., the geometry and material properties of the bead sections are only broadly captured when considering the bead and spring are hooked together and bonded with some sort of adhesive material) [4]. Another potential discrepancy source is manually tuning some of the material parameters, which likely does not arrive at optimal values.

The match with a measurement presented in Fig. 10 sees improvements over several past approaches. In comparison with a response simulated using the simpler spring model with a mass-spring attached at each endpoint [14], additional complexity is captured in the reproduction of secondary chirps and how the response blurs in low-frequency regions, as well as now seeing two harmonic series in the upper frequency region. These can be attributed to the simple model neglecting curvature such that the two transverse spring polarizations become degenerate. As mentioned in the introduction, approaches starting from the Wittrick model have not before incorporated coupling to external components modeling the input and output [20–22]. Improvements from including the beads are seen in the overall amplitude response and the relative levels of different groups of echoes. The main chirps in the reverb tank model (Fig. 10) are dominant because they couple most

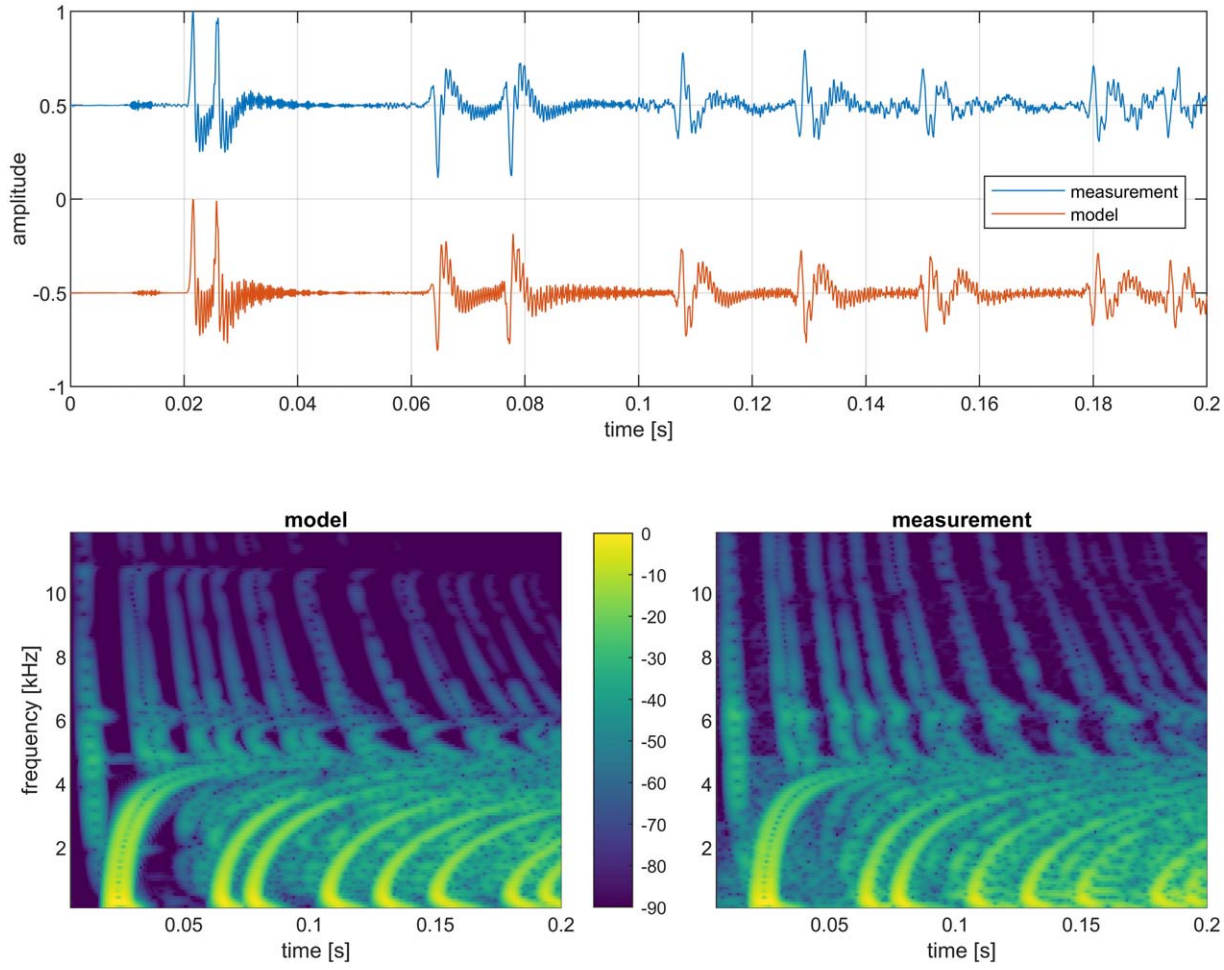


Fig. 10. Impulse response comparison of a modeled and measured spring reverb tank.

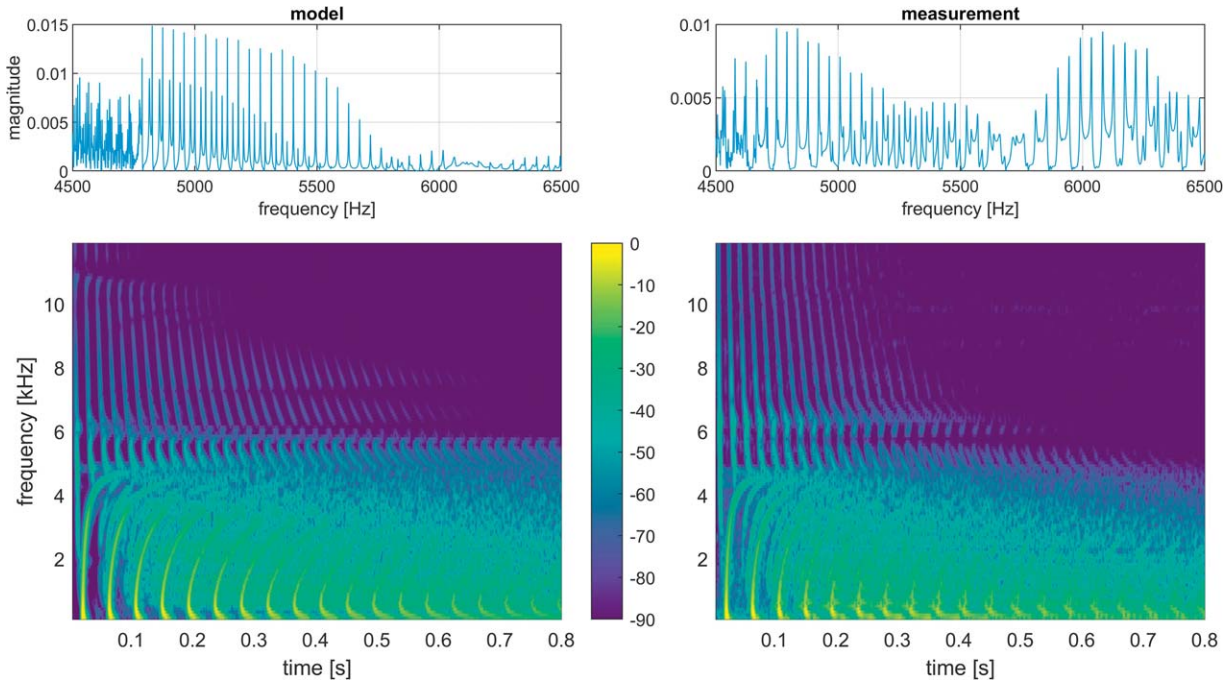


Fig. 11. Impulse response comparison for a single spring in a reverb tank.

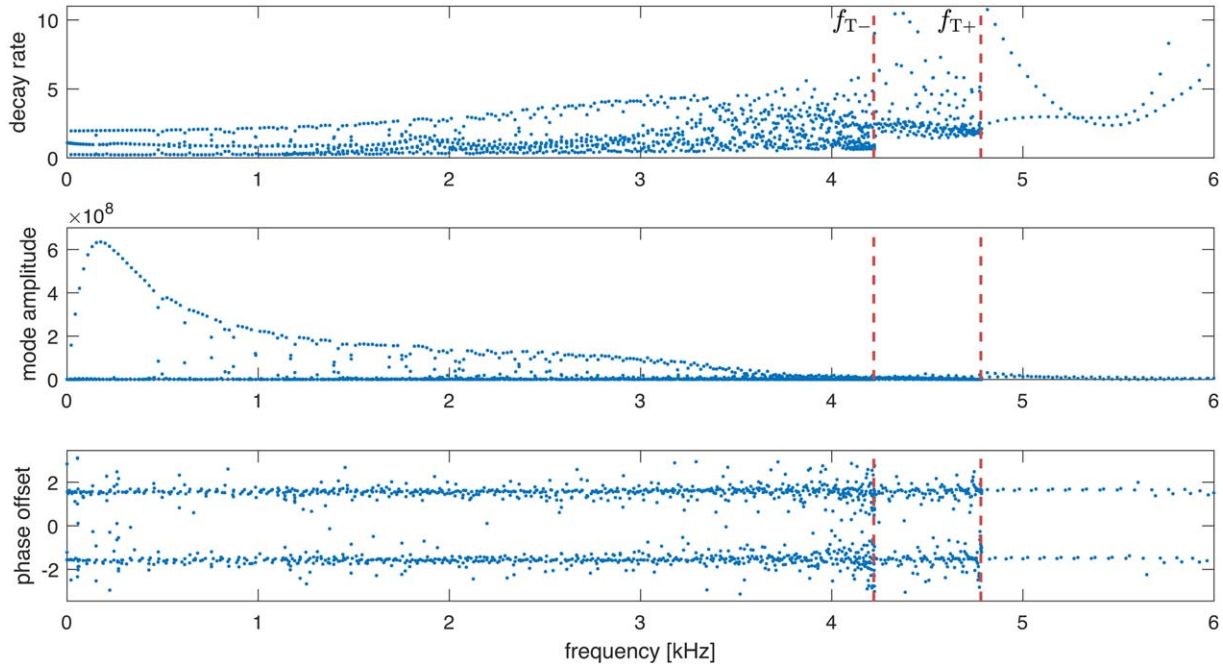


Fig. 12. Modal decay rates, amplitudes, and phase offsets for a tank model using spring 1 in Table 1.

strongly with rotation of the beads, whereas the baseline result (Fig. 9) sees significant contamination (i.e., incorrect mode amplitudes) from other groups of echoes.

Scatter plots of modal decay rate, amplitude, and phase offset each shown against frequency for the single spring are presented in Fig. 12. Formulas for computing modal amplitudes and phase offsets are derived in the Appendix A.2. For the decay plot, five low-frequency modes with extremely high decay rates are considered to contribute relatively little to the impulse response and left out of view. The main observations are a dominant set of amplitudes with a low-pass trend, which likely corresponds to the main chirps, and that multiple decay rates are present within the same frequency range. The latter suggests that the approach of computing the model in lossless form and directly setting modal decay rates, as taken in past studies [21], is no longer straightforward, in that it is unclear how a distribution of modal decay rates as seen in Fig. 12 could be predicted straight from continuous-domain theory. Amplitude and phase offset plots point to the same conclusion: achieving a close match to measurements by manually setting amplitude, phase offset, and decay rate looks nontrivial from the complex behavior shown in Fig. 12.

6 CONCLUSION

A spring reverb tank model is presented here that is the first to consider the magnetic bead dynamics with spring equations that include the effects of helix angle. Careful consideration of the thin form of equations used to model the system, the geometric alignment of the magnetic beads and spring, and the choice of damping parameters for different polarizations yields significant improvements on past research using the thin spring model (as detailed in SEC. 5). The culmination of these modeling choices results in the main features of a measured tank impulse response now being captured well.

One implication of the results, as evident from the mode scatter plots in Fig. 12, is the difficulty of setting amplitude, phase, and decay of oscillators directly to develop a modal algorithm that captures the underlying dynamics without an approach along the lines of the methodology proposed here. In particular, the complex distribution of phase offsets is notable (e.g., when compared to past work on the simple spring model without beads where it only contributed as alternating sign flipping of the amplitudes) [13]. In addition, continuity conditions in the continuous-domain reverb tank model are shown to be lossless through energy analysis, and spectrograms qualitatively confirm the prediction from dispersion analysis that different decay rates exist within narrow frequency bands.

While the numerical approach involves a large matrix eigenvalue computation, an inherently off-line procedure, the final modal-form processing algorithm is well suited to real-time applications since the uncoupled system can make use of parallel computing techniques. Further efficiency considerations in future work include finding new ways to map model parameters to modes extracted from the eigenvalue computation. Considering the heavy computational expense of the diagonalization procedure, the new mappings would avoid recomputing the modes to allow online parameter control. A machine learning approach is well suited to this problem since a comprehensive dataset can be generated using the model over an informed range of parameters. Such an effort would require exploring the large parameter space to identify suitable candidates and ranges for the dataset in the context of effects design—not only for the tank model as presented here but also differ-

ent tank configurations not feasible for exploration with physical reverb tanks.

Once model parameters and ranges are established and can be varied without recomputing modes, developing a real-time audio plugin with time-varying parameters (as, e.g., in [46]) that do not produce artefacts will require a strategy for tracking modes over the parameter space. This is because the complex behavior modal parameters exhibit with frequency, as seen in Fig. 12, means that sorting modes by ascending frequency will not keep the same mode ordering for each parameter setting and could therefore see extreme changes in amplitude or decay rate.

One drawback of the presented methodology lies with the global nature of discretization inherent to the pseudospectral method coupled with the large size of matrices required to capture vibrations in the appropriate frequency range. This can lead to ill-conditioned matrices and numerical precision issues. While such problems can be addressed by increasing the working precision of the eigenvalue computation, a more attractive approach would be adapting the pseudospectral method to the more recently proposed "ultraspherical method" [47]. This follows the standard procedure of spectral methods with the main extension being a change of basis accompanying each differentiation, leveraging the relationships between ultraspherical polynomials such that differentiation matrices are vastly improved in their numerical conditioning.

Further investigative paths look toward improving the coupling between supply current and the force acting on the bead due to the induced magnetic field, which is not considered in depth here and instead accounted for with empirical scaling. In addition, it may be worth considering nonlinear components in the driving/pick-up relating to the coupling between the bead dynamics and the electromagnet. Finally, the damping introduced in the model could be refined through analysis of measured impulse responses.

7 ACKNOWLEDGMENT

This work has been funded in part by the Northern Ireland Department for Economies (DfE) Ph.D. studentship. The authors thank the anonymous reviewers for their time, effort, and constructive input to the manuscript.

8 REFERENCES

[1] L. Hammond, "Electrical Musical Instrument," US Patent 2,230,836 (1941 Feb.).

[2] H. E. Meinema and H. H. Canfield, "Artificial Reverberation Apparatus," US Patent 2,982,819 (1961 May).

[3] H. E. Meinema, H. A. Johnson, and W. C.Jr. Laube, "A New Reverberation Device for High Fidelity Systems," *J. Audio Eng. Soc.*, vol. 9, no. 4, pp. 284–289 (1961 Oct.).

[4] A. C. Young, "Artificial Reverberation Unit," US Patent 3,106,610 (1963 Oct.).

[5] C. O'Donnell, "Why Spring Reverb Will Never Die," *Polyphony*, vol. 8, no. 5, pp. 18–19 (1983 Aug.).

[6] J. Parker and S. Bilbao, "Spring Reverberation: A Physical Perspective," in *Proceedings of the International Conference on Digital Audio Effects (DAFx)*, pp. 416–421 (Como, Italy) (2009 Sep.).

[7] J. S. Abel, S. A. Coffin, and K. S. Spratt, "A Modal Architecture for Artificial Reverberation With Application to Room Acoustics Modeling," presented at the *137th Convention of the Audio Engineering Society* (2014 Oct.), paper 9208.

[8] J. S. Abel and E. K. Canfield-Dafilou, "Dispersive Delay and Comb Filters Using a Modal Structure," *IEEE Signal Process. Lett.*, vol. 26, no. 12, pp. 1748–1752 (2019 Dec.). https://doi.org/10.1109/LSP.2019.2946990.

[9] J. S. Abel, D. P. Berners, S. Costello, and J. O.III Smith, "Spring Reverb Emulation Using Dispersive Allpass Filters in a Waveguide Structure," presented at the *121st Convention of the Audio Engineering Society* (2006 Oct.), paper 6954.

[10] V. Välimäki, J. Parker, and J. S. Abel, "Parametric Spring Reverberation Effect," *J. Audio Eng. Soc.*, vol. 58, no. 7/8, pp. 547–562 (2010 Jul./Aug.).

[11] J. Parker, "Efficient Dispersion Generation Structures for Spring Reverb Emulation," *EURASIP J. Adv. Signal Process.*, vol. 2011, paper 646134 (2011 Mar.). https://doi.org/10.1155/2011/646134.

[12] H. Gamper, J. Parker, and V. Välimäki, "Automated Calibration of a Parametric Spring Reverb Model," in *Proceedings of the International Conference on Digital Audio Effects (DAFx)*, pp. 416–421 (Paris, France) (2011 Sep.).

[13] M. van Walstijn, "Numerical Calculation of Modal Spring Reverb Parameters," in *Proceedings of the International Conference on Digital Audio Effects (DAFx)*, pp. 38–45 (Vienna, Austria) (2020 Sep.).

[14] S. Bilbao and J. Parker, "A Virtual Model of Spring Reverberation," *IEEE Trans. Audio Speech Lang. Process.*, vol. 18, no. 4, pp. 799–808 (2010 May). https://doi.org/10.1109/TASL.2009.2031506.

[15] M. A. Martínez Ramírez, E. Benetos, and J. D. Reiss, "Modeling Plate and Spring Reverberation Using a DSP-Informed Deep Neural Network," in *Proceedings of the IEEE International Conference on Acoustics, Speech and Signal Processing (ICASSP)*, pp. 241–245 (Barcelona, Spain) (2020 May). https://doi.org/10.1109/ICASSP40776.2020.9053093.

[16] F. Papaleo, X. Lizarraga-Seijas, and F. Font, "Evaluating Neural Networks Architectures for Spring Reverb Modelling," in *Proceedings of the International Conference on Digital Audio Effects (DAFx)*, pp. 302–309 (Guildford, UK) (2024 Sep.).

[17] W. H. Wittrick, "On Elastic Wave Propagation in Helical Springs," *Int. J. Mech. Sci.*, vol. 8, no. 1, pp. 25–47 (1966 Jan.). https://doi.org/10.1016/0020-7403(66)90061-0.

[18] T. Tarnopolskaya and F. de Hoog, "Asymptotic Analysis of the Free In-Plane Vibrations of Beams With Arbitrarily Varying Curvature and Cross-Section," *J. Sound Vib.*, vol. 196, no. 5, pp. 659–680 (1996 Oct.). https://doi.org/10.1006/jsvi.1996.0507.

[19] S. Bilbao and J. Parker, "Perceptual and Numerical Aspects of Spring Reverberation Modeling," in

Proceedings of the International Symposium on Musical Acoustics (ISMA), pp. 151–158 (Sydney, Australia) (2010 Aug.).

[20] S. Bilbao, "Numerical Simulation of Spring Reverberation," in *Proceedings of the International Conference on Digital Audio Effects (DAFx)*, paper 19 (Maynooth, Ireland) (2013 Sep.).

[21] J. McQuillan and M. van Walstijn, "Modal Spring Reverb Based on Discretisation of the Thin Helical Spring Model," in *Proceedings of the International Conference on Digital Audio Effects (DAFx)*, pp. 191–198 (Vienna, Austria) (2021 Sep.).

[22] J. McQuillan and M. van Walstijn, "Helical Spring Mode Grouping," in *Proceedings of the Stockholm Music Acoustics Conference (SMAC)*, pp. 43–50 (Stockholm, Sweden) (2023 Jun.).

[23] J. McQuillan, M. van Walstijn, J. D. Parker, and M. Ortiz, "Experimental Investigation of the Driving Mechanism in Spring Reverberation Tanks," in *Proc. Mtgs. Acoust.*, vol. 49, paper 035007 (2022 Dec.). https://doi.org/10.1121/2.0001662.

[24] J. Lee, "Free Vibration Analysis of Cylindrical Helical Springs by the Pseudospectral Method," *J. Sound Vib.*, vol. 302, no. 1–2, pp. 185–196 (2007 Jan.). https://doi.org/10.1016/j.jsv.2006.11.008.

[25] D. Pearson, "The Transfer Matrix Method for the Vibration of Compressed Helical Springs," *J. Mech. Eng. Sci.*, vol. 24, no. 4, pp. 163–171 (1982 Dec.). https://doi.org/10.1243/JMES_JOUR_1982_024_033_02.

[26] V. Yıldırım, "An Efficient Numerical Method for Predicting the Natural Frequencies of Cylindrical Helical Springs," *Int. J. Mech. Sci.*, vol. 41, no. 8, pp. 919–939 (1999 Aug.). https://doi.org/10.1016/S0020-7403(98)00065-4.

[27] J. Lee and D. J. Thompson, "Dynamic Stiffness Formulation, Free Vibration and Wave Motion of Helical Springs," *J. Sound Vib.*, vol. 239, no. 2, pp. 297–320 (2001 Jan.). https://doi.org/10.1006/jsvi.2000.3169.

[28] J. E. Mottershead, "Finite Elements for Dynamical Analysis of Helical Rods," *Int. J. Mech. Sci.*, vol. 22, no. 5, pp. 267–283 (1980 Oct.). https://doi.org/10.1016/0020-7403(80)90028-4.

[29] R. L. Wegel, "Wave Transmission Device," US Patent 1,852,795 (1932 Apr.).

[30] A. M. Wahl, *Mechanical Springs* (McGraw-Hill, New York, NY, 1963), 2nd ed.

[31] L. E. Becker, G. G. Chassie, and W. L. Cleghorn, "On the Natural Frequencies of Helical Compression Springs," *Int. J. Mech. Sci.*, vol. 44, no. 4, pp. 825–841 (2002 Apr.). https://doi.org/10.1016/S0020-7403(01)00096-0.

[32] R. S. Lakes, *Viscoelastic Solids* (CRC Press, Boca Raton, FL, 1999).

[33] S. V. Sorokin, "Linear Dynamics of Elastic Helical Springs: Asymptotic Analysis of Wave Propagation," *Proc. R. Soc. A*, vol. 465, no. 2105, pp. 1513–1537 (2009 May). https://doi.org/10.1098/rspa.2008.0468.

[34] J. W. S. Rayleigh, *The Theory of Sound* (New York: Dover Publications, New York, NY, 1945), 2nd ed.

[35] K. F. Graff, *Wave Motion in Elastic Solids* (Dover Publications, New York, NY, 1975).

[36] S. Bilbao, *Numerical Sound Synthesis* (Wiley, Chichester, UK, 2009). https://doi.org/10.1002/9780470749012.

[37] J. P. Boyd, *Chebyshev and Fourier Spectral Methods* (Dover Publications, New York, NY, 2001).

[38] L. N. Trefethen, *Spectral Methods in MATLAB* (Society for Industrial and Applied Mathematics, Philadelphia, PA, 2000). https://doi.org/10.1137/1.9780898719598.

[39] B. Fornberg, *A Practical Guide to Pseudospectral Methods* (Cambridge University Press, Cambridge, UK, 1998). https://doi.org/10.1017/CBO9780511626357.

[40] T. A. Driscoll, N. Hale, and L. N. Trefethen, *Chebfun Guide* (Pafnuty Publications, Oxford, UK, 2014).

[41] L. N. Trefethen, *Approximation Theory and Approximation Practice* (Society for Industrial and Applied Mathematics, Philadelphia, PA, 2013).

[42] K. A. Foss, "Co-Ordinates Which Uncouple the Equations of Motion of Damped Linear Dynamic Systems," *J. App. Mech.*, vol. 25, no. 3, pp. 361–364 (1958 Sep.). https://doi.org/10.1115/1.4011828.

[43] S. Krenk, "Complex Modes and Frequencies in Damped Structural Vibrations," *J. Sound Vib.*, vol. 270, no. 4–5, pp. 981–996 (2004 Mar.). https://doi.org/10.1016/S0022-460X(03)00768-5.

[44] J. G. Proakis and D. G. Manolakis, *Digital Signal Processing: Principles, Algorithms, and Applications* (Prentice-Hall, Upper Saddle River, NJ, 1992).

[45] P. R. Karam and B. Bamieh, "Implicit Boundary Conditions in Partial Differential Equations Discretizations: Identifying Spurious Modes and Model Reduction," *J. Comp. Phys.*, vol. 500, paper 112743 (2024 Mar.). https://doi.org/10.1016/j.jcp.2023.112743.

[46] M. G. Onofrei, S. Willemsen, and S. Serafin, "Implementing Physical Models in Real-Time using Partitioned Convolution: An Adjustable Spring Reverb," in *Proceedings of the Sound and Computing Music Conference (SMC)*, pp. 108–114 (Online) (2021 Jun./Jul.).

[47] S. Olver and A. Townsend, "A Fast and Well-Conditioned Spectral Method," *SIAM Rev.*, vol. 55, no. 3, pp. 462–489 (2013 Sep.). https://doi.org/10.1137/120865458.

A.1 THIN SPRING MODEL ENERGY BALANCE

The short derivation here outlines the path from helical spring equations to their energy balance in Eq. (25). For readability, dot notation is adopted to denote differentiation in time: $\dot{u} = \partial_t u$. The l_2 inner products and accompanying norms are defined as in [36]:

$$\langle u, v \rangle_{\mathcal{D}} = \int_0^L uv \, ds, \quad \|u\| = \sqrt{\langle u, u \rangle_{\mathcal{D}}}, \tag{80}$$

where $\mathcal{D} \in \begin{bmatrix} 0 & L \end{bmatrix}$. Again for readability, the 5 subscript has been dropped: all expressions below apply to the thin spring in isolation. Taking inner products with velocity

terms for each of the thin spring equations in turn is as follows:

$$\rho A\ddot{\mathbf{x}} = \mathbf{A}\mathbf{p} + \mathbf{B}\mathbf{q} - \begin{bmatrix}\sigma_u \\ \sigma_v\end{bmatrix}\dot{\mathbf{x}}, \tag{81}$$

$$\begin{aligned}\rho A\left(\langle \dot{u}, \ddot{u}\rangle_{\mathcal{D}} + \langle \dot{v}, \ddot{v}\rangle_{\mathcal{D}}\right) &= \left[\dot{u}p_u + \dot{v}p_v\right]_{\mathcal{D}} - \sigma_u\langle \dot{u}, \dot{u}\rangle_{\mathcal{D}} \\ &- \sigma_v\langle \dot{v}, \dot{v}\rangle_{\mathcal{D}} - \langle \partial_s\dot{u}, p_u\rangle_{\mathcal{D}} - \tau\langle \dot{u}, p_v\rangle_{\mathcal{D}} + \tau\langle \dot{v}, p_u\rangle_{\mathcal{D}} \\ &- \langle \partial_s\dot{v}, p_v\rangle_{\mathcal{D}} + \kappa\langle \dot{u}, p_w\rangle_{\mathcal{D}}.\end{aligned} \tag{82}$$

$$\mathbf{C}\ddot{\mathbf{y}} = \mathbf{K}\mathbf{m} - \mathbf{B}\mathbf{p} + \partial_s\mathbf{q} - \begin{bmatrix}\sigma_w \\ \sigma_\theta\end{bmatrix}\dot{\mathbf{y}}, \tag{83}$$

$$\begin{aligned}\rho A\langle \dot{w}, \ddot{w}\rangle_{\mathcal{D}} + 2\rho I\langle \dot{\theta}_w, \ddot{\theta_w}\rangle_{\mathcal{D}} &= \left[\dot{w}p_w + \dot{\theta}_w m_w\right]_{\mathcal{D}} \\ &- \sigma_w\langle \dot{w}, \dot{w}\rangle_{\mathcal{D}} - \sigma_\theta\langle \dot{\theta}_w, \dot{\theta}_w\rangle_{\mathcal{D}} - \kappa\langle \dot{\theta}_w, m_u\rangle_{\mathcal{D}} \\ &- \kappa\langle \dot{w}, p_u\rangle_{\mathcal{D}} - \langle \partial_s\dot{w}, p_w\rangle_{\mathcal{D}} - \langle \partial_s\dot{\theta}_w, m_w\rangle_{\mathcal{D}}.\end{aligned} \tag{84}$$

$$\mathbf{A}\mathbf{m} = \mathbf{H}\mathbf{p} + \mathbf{K}^{\intercal}\mathbf{q}, \tag{85}$$

$$\begin{aligned}0 &= \left[\dot{\theta}_u m_u + \dot{\theta}_v m_v\right]_{\mathcal{D}} - \langle \partial_s\dot{\theta}_u, m_u\rangle_{\mathcal{D}} - \tau\langle \dot{\theta}_u, m_v\rangle_{\mathcal{D}} \\ &+ \tau\langle \dot{\theta_v}, m_u\rangle_{\mathcal{D}} - \langle \partial_s\dot{\theta_v}, m_v\rangle_{\mathcal{D}} - \langle \dot{\theta}_u, p_v\rangle_{\mathcal{D}} \\ &+ \langle \dot{\theta_v}, p_u\rangle_{\mathcal{D}} + \kappa\langle \dot{\theta}_u, m_w\rangle_{\mathcal{D}}.\end{aligned} \tag{86}$$

$$\mathbf{A}\mathbf{x} = \mathbf{H}\,\boldsymbol{\theta} - \mathbf{B}\mathbf{y}, \tag{87}$$

$$\begin{aligned}0 &= \langle p_u, \partial_s\dot{u}\rangle_{\mathcal{D}} - \tau\langle p_u, \dot{v}\rangle_{\mathcal{D}} + \tau\langle p_v, \dot{u}\rangle_{\mathcal{D}} + \langle p_v, \partial_s\dot{v}\rangle_{\mathcal{D}} \\ &- \langle p_u, \dot{\theta}_v\rangle_{\mathcal{D}} + \langle p_v, \dot{\theta}_u\rangle_{\mathcal{D}} + \kappa\langle p_u, \dot{w}\rangle_{\mathcal{D}}.\end{aligned} \tag{88}$$

$$\mathbf{A}\,\boldsymbol{\theta} = \mathbf{K}^{\intercal}\mathbf{y} + \frac{\mathbf{m}}{(E + \eta\partial_t)\,I}, \tag{89}$$

$$\begin{aligned}\frac{1}{EI}\left(\langle m_u, \dot{m}_u\rangle_{\mathcal{D}} + \langle m_v, \dot{m}_v\rangle_{\mathcal{D}}\right) &= \frac{\eta}{E}\left[m_u\ddot{\theta}_u + m_v\ddot{\theta}_v\right]_{\mathcal{D}} \\ &+ \langle m_u, \partial_s\dot{\theta}_u\rangle_{\mathcal{D}} - \tau\langle m_u, \dot{\theta}_v\rangle_{\mathcal{D}} + \tau\langle m_v, \dot{\theta}_u\rangle_{\mathcal{D}} \\ &+ \langle m_v, \partial_s\dot{\theta}_v\rangle_{\mathcal{D}} + \kappa\langle m_u, \dot{\theta}_w\rangle_{\mathcal{D}} + \frac{\eta}{E}\Big(-\langle \partial_s m_u, \ddot{\theta}_u\rangle_{\mathcal{D}} \\ &- \tau\langle m_u, \ddot{\theta}_v\rangle_{\mathcal{D}} + \tau\langle m_v, \ddot{\theta}_u\rangle_{\mathcal{D}} - \langle \partial_s m_v, \ddot{\theta}_v\rangle_{\mathcal{D}} \\ &+ \kappa\langle m_u, \ddot{\theta}_w\rangle_{\mathcal{D}}\Big).\end{aligned} \tag{90}$$

$$\partial_s\mathbf{y} = \mathbf{B}\mathbf{x} - \mathbf{K}\,\boldsymbol{\theta} + \mathbf{J}\mathbf{q}, \tag{91}$$

$$\begin{aligned}\frac{1}{EA}\langle p_w, \dot{p}_w\rangle_{\mathcal{D}} + \frac{1}{2GI}\langle m_w, \dot{m}_w\rangle_{\mathcal{D}} &= \frac{\eta}{E}\left[p_w\ddot{w} + m_w\ddot{\theta}_w\right]_{\mathcal{D}} \\ &+ \langle p_w, \partial_s\dot{w}\rangle_{\mathcal{D}} + \langle m_w, \partial_s\dot{\theta}_w\rangle_{\mathcal{D}} - \kappa\langle p_w, \dot{u}\rangle_{\mathcal{D}} \\ &- \kappa\langle m_w, \dot{\theta}_u\rangle_{\mathcal{D}} + \frac{\eta}{E}\Big(-\langle \partial_s p_w, \ddot{w}\rangle_{\mathcal{D}} - \langle \partial_s m_w, \ddot{\theta}_w\rangle_{\mathcal{D}} \\ &- \kappa\langle p_w, \ddot{u}\rangle_{\mathcal{D}} - \kappa\langle m_w, \ddot{\theta}_u\rangle_{\mathcal{D}}\Big).\end{aligned} \tag{92}$$

Combining the separate expressions sees cancellation of 16 pairs of opposite signed inner product terms (all those without η). The left hand side terms of each equation represent the change over time of the spring energy defined in Eq. (26). Thus, the following can be written:

$$\dot{\mathcal{H}} = \mathcal{X} - \mathcal{Y} + \mathcal{Z}, \tag{93}$$

where

$$\begin{aligned}\mathcal{X} = \Bigg[&\dot{u}p_u + \dot{v}p_v + \dot{w}p_w + \dot{\theta}_u m_u + \dot{\theta}_v m_v + \dot{\theta}_w m_w \\ &+ \frac{\eta}{E}\Big(\ddot{w}p_w + \ddot{\theta}_u m_u + \ddot{\theta}_v m_v + \ddot{\theta}_w m_w\Big)\Bigg]_{\mathcal{D}},\end{aligned} \tag{94}$$

$$\mathcal{Y} = \frac{\sigma_u}{2}\|\dot{u}\|^2 + \frac{\sigma_v}{2}\|\dot{v}\|^2 + \frac{\sigma_w}{2}\|\dot{w}\|^2 + \frac{\sigma_\theta}{2}\|\dot{\theta}_w\|^2, \tag{95}$$

$$\begin{aligned}\mathcal{Z} = -\frac{\eta}{E}\Big(&\langle \partial_s m_u, \ddot{\theta}_u\rangle_{\mathcal{D}} + \tau\langle m_u, \ddot{\theta}_v\rangle_{\mathcal{D}} - \tau\langle m_v, \ddot{\theta}_u\rangle_{\mathcal{D}} \\ &+ \langle \partial_s m_v, \ddot{\theta}_v\rangle_{\mathcal{D}} - \kappa\langle m_u, \ddot{\theta}_w\rangle_{\mathcal{D}} + \langle \partial_s p_w, \ddot{w}\rangle_{\mathcal{D}} \\ &+ \langle \partial_s m_w, \ddot{\theta}_w\rangle_{\mathcal{D}} + \kappa\langle p_w, \ddot{u}\rangle_{\mathcal{D}} + \kappa\langle m_w, \ddot{\theta}_u\rangle_{\mathcal{D}}\Big).\end{aligned} \tag{96}$$

Arriving at the final energy balance requires substitutions using the thin spring equations, but only for the terms in $\mathcal{Z}$:

$$\begin{aligned}\mathcal{Z} = -\frac{\eta}{E}\Big(&\langle \underbrace{\partial_s m_u - \tau m_v + \kappa m_w}_{p_v}, \ddot{\theta}_u\rangle_{\mathcal{D}} \\ &+ \langle \underbrace{\tau m_u + \partial_s m_v}_{-p_u}, \ddot{\theta}_v\rangle_{\mathcal{D}} + \langle \underbrace{\partial_s m_w - \kappa m_u}_{2\rho I\ddot{\theta}_w}, \ddot{\theta}_w\rangle_{\mathcal{D}} \\ &+ \langle \underbrace{\partial_s p_w}_{\kappa p_u + \rho A\ddot{w}}, \ddot{w}\rangle_{\mathcal{D}}\rangle + \langle \underbrace{\kappa p_w}_{-\partial_s p_u + \tau p_v + \rho A\ddot{u}}, \ddot{u}\rangle_{\mathcal{D}}\Big),\end{aligned} \tag{97}$$

which becomes

$$\begin{aligned}\mathcal{Z} = -\frac{\eta}{E}\Big(&\langle p_v, \ddot{\theta}_u\rangle_{\mathcal{D}} - \langle p_u, \ddot{\theta}_v\rangle_{\mathcal{D}} + \rho I\|\ddot{\theta}_w\|^2 \\ &+ \frac{\rho A}{2}\left(\|\ddot{u}\|^2 + \|\ddot{w}\|^2\right) + \langle \kappa p_u, \ddot{w}\rangle_{\mathcal{D}} - \langle \partial_s p_u, \ddot{u}\rangle_{\mathcal{D}} \\ &+ \langle \tau p_v, \ddot{u}\rangle_{\mathcal{D}}\Big).\end{aligned} \tag{98}$$

Applying integration by parts to the penultimate term and making further substitutions yields

$$\begin{aligned}\mathcal{Z} = -\frac{\eta}{E}\Big(&\frac{\rho A}{2}\left(\|\ddot{u}\|^2 + \|\ddot{w}\|^2\right) + \rho I\|\ddot{\theta}_w\|^2 - [\ddot{u}p_u]_{\mathcal{D}} \\ &+ \langle p_v, \ddot{\theta}_u\rangle_{\mathcal{D}} - \langle p_u, \ddot{\theta}_v\rangle_{\mathcal{D}} + \langle p_u, \underbrace{\kappa\ddot{w}}_{-\partial_s\ddot{u} + \tau\ddot{v} + \ddot{\theta}_v}\rangle_{\mathcal{D}} \\ &+ \langle p_u, \partial_s\ddot{u}\rangle_{\mathcal{D}} + \langle p_v, \underbrace{\tau\ddot{u}}_{-\partial_s\ddot{v} - \ddot{\theta}_u}\rangle_{\mathcal{D}}\Big),\end{aligned} \tag{99}$$

which sees cancellation of three more pairs of inner product terms:

$$\begin{aligned}\mathcal{Z} = -\frac{\eta}{E}\Big(&\frac{\rho A}{2}\left(\|\ddot{u}\|^2 + \|\ddot{w}\|^2\right) + \rho I\|\ddot{\theta}_w\|^2 - [\ddot{u}p_u]_{\mathcal{D}} \\ &+ \langle \tau p_u, \ddot{v}\rangle_{\mathcal{D}} - \langle p_v, \partial_s\ddot{v}\rangle_{\mathcal{D}}\Big).\end{aligned} \tag{100}$$

Another application of integration by parts to the last term allows a final substitution after combining the remaining

inner product terms:

$$\mathcal{Z} = -\frac{\eta}{E}\Big(\frac{\rho A}{2}\big(\|\ddot{u}\|^2 + \|\ddot{w}\|^2\big) + \rho I\|\ddot{\theta}_w\|^2 - \big[\ddot{u}\,p_u + \ddot{v}\,p_v\big]_{\mathcal{D}} + \langle \underbrace{\tau p_u + \partial_s p_v}_{\rho A\ddot{v}}, \ddot{v}\rangle_{\mathcal{D}}\Big), \tag{101}$$

and this substitution then gives the final form of $\mathcal{Z}$:

$$\mathcal{Z} = -\frac{\eta}{E}\Big(\frac{\rho A}{2}\big(\|\ddot{u}\|^2 + \|\ddot{v}\|^2 + \|\ddot{w}\|^2\big) + \rho I\|\ddot{\theta}_w\|^2 - [\ddot{u}\,p_u + \ddot{v}\,p_v]_{\mathcal{D}}\Big). \tag{102}$$

Using this form of $\mathcal{Z}$ in the energy balance expression Eq. (93) makes it equivalent to the thin spring energy balance presented in Eq. (25).

A.2 MODAL OSCILLATORS INCORPORATING A PHASE OFFSET

To demonstrate that a phase offset is included in modal oscillators, a single impulse response expression $h(t)$ is derived instead of the separate expressions $h_{\mathrm{p}}(t)$ and $h_{\mathrm{q}}(t)$ in Eqs. (70) and (71). First, substituting P and Q defined in Eqs. (67) and (68) into the transfer function $H(\hat{s})$ in Eq. (69) yields

$$H_i(\hat{s}) = \frac{(\hat{s}+\tilde{\alpha}_i)\left(c_{\mathrm{in,p},i}c_{\mathrm{out,p},i} + c_{\mathrm{in,q},i}c_{\mathrm{out,q},i}\right)}{(\hat{s}+\tilde{\alpha}_i)^2 + \omega_{\mathrm{r},i}^2} + \frac{\omega_{\mathrm{r},i}\left(c_{\mathrm{in,q},i}c_{\mathrm{out,p},i} - c_{\mathrm{in,p},i}c_{\mathrm{out,q},i}\right)}{(\hat{s}+\tilde{\alpha}_i)^2 + \omega_{\mathrm{r},i}^2}. \tag{103}$$

Taking the inverse Laplace transform then gives an oscillator impulse response expression:

$$h_i(t) = \mathrm{e}^{-\tilde{\alpha}_i t}\Big[c_{1,i}\cos\left(\omega_{\mathrm{r},i}t\right) + c_{2,i}\sin\left(\omega_{\mathrm{r},i}t\right)\Big], \tag{104}$$

where

$$c_{1,i} = c_{\mathrm{in,p},i}c_{\mathrm{out,p},i} + c_{\mathrm{in,q},i}c_{\mathrm{out,q},i}, \tag{105}$$

$$c_{2,i} = c_{\mathrm{in,q},i}c_{\mathrm{out,p},i} - c_{\mathrm{in,p},i}c_{\mathrm{out,q},i}. \tag{106}$$

This can be written as a single sine expression:

$$h_i(t) = \mathrm{e}^{-\tilde{\alpha}_i t}c_i\sin\left(\omega_{\mathrm{r},i}t + \phi_i\right), \tag{107}$$

with the overall modal amplitude c_i and phase offset ϕ_i defined as

$$c_i = \sqrt{c_{1,i}^2 + c_{2,i}^2}, \tag{108}$$

$$\phi_i = \arctan\left(\frac{c_{1,i}}{c_{2,i}}\right) + \left[\frac{1}{2} - \frac{1}{2}\mathrm{sign}\left(c_{2,i}\right)\right]\pi, \tag{109}$$

where the second term in the last equation is included to account for both negative and positive $c_{2,\,i}$ values.

THE AUTHORS


Jacob McQuillan


Maarten van Walstijn


Julian D. Parker


Miguel Ortiz

Jacob McQuillan holds a B.Sc. degree in Audio Engineering (2020) and M.Res. degree related to physical modeling sound synthesis (2021), both from the Centre for Interdisciplinary Research in Sound and Music (SARC) of Queen's University Belfast. He is currently working toward his Ph.D. at SARC, focusing on physical modeling of spring reverberation. His research interests center around numerical modeling of analog audio equipment and musical instruments.

•

Maarten van Walstijn is a graduate of the Institute of Sonology in The Hague (The Netherlands). He obtained a Ph.D. at the University of Edinburgh in 2002 and was a postdoctoral research assistant from 2001 to 2003. Currently, he is Senior Lecturer at the School of Electronics, Electric Engineering, and Computer Science of Queen's University Belfast. He conducts his research at the Centre for Interdisciplinary Research in Sound and Music (SARC) in the interdisciplinary field of music, audio signal processing, and acoustics, working on a variety of related topics, including physics-based sound synthesis, musical instrument acoustics, virtual analog modeling, sensor interface design, room acoustics modeling, spatial audio, and audio for virtual reality.

•

Julian Parker, born in the United Kingdom, holds a B.A. (Hons.) in natural sciences from the University of Cambridge, UK (2005), M.Sc. in acoustics and music technology from the University of Edinburgh, UK (2008), and D.Sc. (Tech.) in audio signal processing and acoustics from Aalto University, Finland (2013). His doctoral work focused on computational modeling of dispersive physical systems in the audio frequency range. He has held leadership positions in industrial research at companies such as Native Instruments, TikTok, and Stability AI, focusing on processing and generating of musical sound using both traditional signal processing techniques, machine learning, and artificial intelligence. His current research interests are in generative modeling of musical audio and in the intersection between signal processing and neural network structures.

•

Miguel Ortiz is a Mexican composer, sound artist, and digital instrument maker. He graduated in composition at the Conservatorio de las Rosas, Morelia, Mexico (2005) and holds an M.A. (2006) and Ph.D. (2010) in Sonic Arts from Queen's University Belfast. His research explores a vast array of performing mediums ranging from traditional acoustic instruments such as cello and trumpet to laptop improvisation, performance with bio-instruments, and hyperinstruments. Ortiz brings expertise on novel instrument design and the broader ecosystems in which musical instruments are used for improvisation and composition. His research contains a particular interest in chaotic systems and the tension between control and emergence in musical expression.